Persistent anticyclonic conditions and climate change exacerbated the exceptional 2022 European-Mediterranean drought

Davide Faranda, Salvatore Pascale, Burak Bulut

▶ **To cite this version:**

Davide Faranda, Salvatore Pascale, Burak Bulut. Persistent anticyclonic conditions and climate change exacerbated the exceptional 2022 European-Mediterranean drought. Environmental Research Letters, 2023, 18 (3), pp.034030. 10.1088/1748-9326/acbc37 . hal-03907855v2

HAL Id: hal-03907855

https://hal.science/hal-03907855v2

Submitted on 13 Feb 2023 (v2), last revised 24 Mar 2023 (v3)

HAL is a multi-disciplinary open access archive for the deposit and dissemination of scientific research documents, whether they are published or not. The documents may come from teaching and research institutions in France or abroad, or from public or private research centers.

L'archive ouverte pluridisciplinaire **HAL**, est destinée au dépôt et à la diffusion de documents scientifiques de niveau recherche, publiés ou non, émanant des établissements d'enseignement et de recherche français ou étrangers, des laboratoires publics ou privés.

Persistent anticyclonic conditions and climate change exacerbated the exceptional 2022 European-Mediterranean drought

Davide Faranda[1,2,3,*], **Salvatore Pascale**[4,5,*], **Burak Bulut**[1,*]

[1] Laboratoire des Sciences du Climat et de l'Environnement, UMR 8212 CEA-CNRS-UVSQ, Université Paris-Saclay & IPSL, CE Saclay l'Orme des Merisiers, 91191, Gif-sur-Yvette, France

[2] London Mathematical Laboratory, 8 Margravine Gardens, London, W6 8RH, British Islands

[3] Laboratoire de Météorologie Dynamique/IPSL, École Normale Supérieure, PSL Research University, Sorbonne Université, École Polytechnique, IP Paris, CNRS, 75005, Paris, France

[4] University of Bologna, Department of Physics and Astronomy, 40126, Bologna, Italy

[5] Centre for Sustainability and Climate Change, Bologna Business School, 40136, Bologna, Italy

[*] All authors have equally contributed to this work

E-mail: `davide.faranda@cea.fr, salvatore.pascale@unibo.it, burak.bulut@cea.fr`

13 February 2023

Abstract. A prolonged drought affected Western Europe and the Mediterranean region in 2022 producing large socio-ecological impacts. The role of anthropogenic climate change (ACC) in exacerbating this drought has been often invoked in the public debate, but the link between atmospheric circulation and ACC has not received much attention so far. Here we address this question by applying the method of circulation analogs, which allows us to identify atmospheric patterns in the period 1836-2021 very similar to those occurred in 2022. By comparing the circulation analogs when global warming was absent (1836-1915) with those occurred recently (1942-2021), and by excluding interannual and interdecadal variability as possible drivers, we identify the contribution of ACC. The 2022 drought was associated with a persistent anticyclonic anomaly over Western Europe. Circulation analogs of this atmospheric pattern in 1941-2021 feature 500 hPa geopotential height anomalies larger in both extent and magnitude, and higher temperatures at the surface, relative to those in 1836-1915. Both factors exacerbated the drought, by increasing the area affected and enhancing soil drying through evapotranspiration. While the occurrence of the atmospheric circulation associated with the 2022 drought has not become more frequent in recent decades, the influence of the Atlantic Multidecadal oscillation cannot be ruled-out.

Keywords: Drought - Climate Change - Attribution

1. Characteristics of the 2022 Euro-Mediterranean drought

Intense and prolonged drought conditions affected large portions of France, Italy, and Spain throughout most of 2022. The drought, related to a persistent lack of precipitation in the last months of 2021, became evident in northwestern Italy since March 2022 [1] and then expanded to western Europe in the following months. The severity of the drought then further worsened during spring and summer 2022 (Fig.1b), due to a persistent lack of precipitation combined with a sequence of heatwaves from May onwards [2, 3] which further dried the soil through enhanced evapotranspiration [4]. Using the Standardized Precipitation Evapotranspiration Index aggregated at 9 months (SPEI9) to monitor and characterize the 2022 drought [4, 5], we show in Fig.1c,d the record-breaking negative values of the drought indicator SPEI9 in August 2022 (see Sect.2.1 for details about SPEI) over southern France and Northern Italy. The area-average of SPEI9 over the two areas was consistently below -2 (extreme drought), with local grid points having SPEI9 values below -3.

The socio-ecological impacts of the 2022 drought have been severe in Italy, France and Spain. The exceptionality of the water and heat stress substantially reduced yields of some of the main crops like, e.g., grain maize, soybean, and sunflowers, with reductions of around 15% relative to the last 5-year average [6]. In Italy, about 50% of the population was affected by the drought emergency water restrictions, especially in the North of the country. The Po river basin Authority reported record-breaking levels of inland salt intrusion from the Po delta up to 40 km from the sea coast. Reduced stored water severely impacted the energy sector for both hydropower generation and cooling systems of other power plants in the north of the country. In southern France, wildfires associated with the extreme drought conditions were also more widespread, with a surface of burned land more than double than in 2021 and about 4.6 times the average of the period 2012-2021. Sixty-six French "departments" were at the highest drought warning level in August, with at least ninety-three departments at one of the top three levels of warning for drought. Similar impacts on agriculture, energy production and domestic water usage were reported in Spain, Portugal and Netherlands too [2].

While drought is a complex phenomenon [7, 8], whose intensity can be exacerbated by non-trivial land surface-atmosphere feedbacks and land usage [9], the large scale atmospheric circulation played a key role in driving the 2022 Euro-Mediterranean drought. This is evident when examining the mean December 2021-August 2022 circulation anomalies: a persistent high pressure anomaly centered over France is visible both in the lower and middle troposphere (Fig.1a). This circulation anomaly favored meteorological conditions characterized by stable conditions with no precipitation over large swaths of Europe.

The 2022 Euro-Mediterranean drought unfolded as El Niño-Southern Oscillation (ENSO) was in a persistent negative phase (La Niña) since the summer of 2020. It is therefore natural to ask whether La Niña did play a role in remotely driving the long-lasting anticyclonic circulation. The relationship between ENSO and the North

Atlantic-European sector is not as well defined as for other regions of the world, and probably non-stationary in time [10, 11, 12]. If we compare the slow-evolving circulation anomaly of 2022 in Europe with that of other years featuring similar 3-year La Niña conditions (i.e., 1956, 1975, and 2000), we see large differences in the intensity and spatial patterns of the anomalies and no resemblance to the 2022 pattern (Fig. S1). This leads us to conjecture that there might not be a simple causality relationship between La Niña and the persistent anticyclonic anomaly observed over western Europe in 2022, although this is a point that we will further investigate in this study.

The 2022 drought had large societal impacts rising the attention of the media at the national and international levels [13, 14, 15, 3] and putting water management high on the agenda of water managers and decision-makers. Questions on the role played by the ongoing anthropogenic climate change (ACC) on this drought, and eventually on future droughts, are therefore pressing in the media debate, and answers to these questions are urgent to manage future similar water crises. Specifically, the questions we ask here are: how rare was the prolonged atmospheric circulation anomaly that drove the 2022 drought situation? Was such anomaly changed in shape, intensity, and thermal structure because of ACC, thus exacerbating similar drought events?

In this study, we address these questions through the method of the analogs of circulation for extreme event attribution [16, 17]. We use the implementation developed by [18] for short-lived meteorological events of a few days of duration (e.g., cyclones, hot and cold spells, etc.), which we adapt to account for long-lasting events such as droughts. For the construction of factual and counterfactual climate [19], we rely on long-term monthly reanalyses (1836 to present) that allow for the construction of robust statistics. We, therefore, compare analogs of this averaged circulation in factual (1836-1915) and counterfactual (1941-2021) periods and study the associated temperature, precipitation, and SPEI9, looking for statistically significant differences that can then be attributed to climate change. Other complementary approaches for event attribution of extreme drought rely on single model initial-condition large ensembles [20, 21, 22]. While a model ensemble approach allows for a clear separation of counterfactual vs factual climate, it still suffers from model biases that can limit the realism of the results. Therefore in this study, we focus on reanalysis only, planning to analyze models as a second step.

2. Methods and Data

2.1. Drought and circulation variables

To capture the 2022 drought condition, we use the Standardized Precipitation Evapotranspiration Index [4, 5] aggregated at 9 months (SPEI9) as the 9-month aggregation timescale roughly corresponds to the period of negative precipitation deficit observed over western Europe. The SPEI generalizes the Standard Precipitation Index (SPI, [23]) by taking into account surface temperature too through its effects on Potential

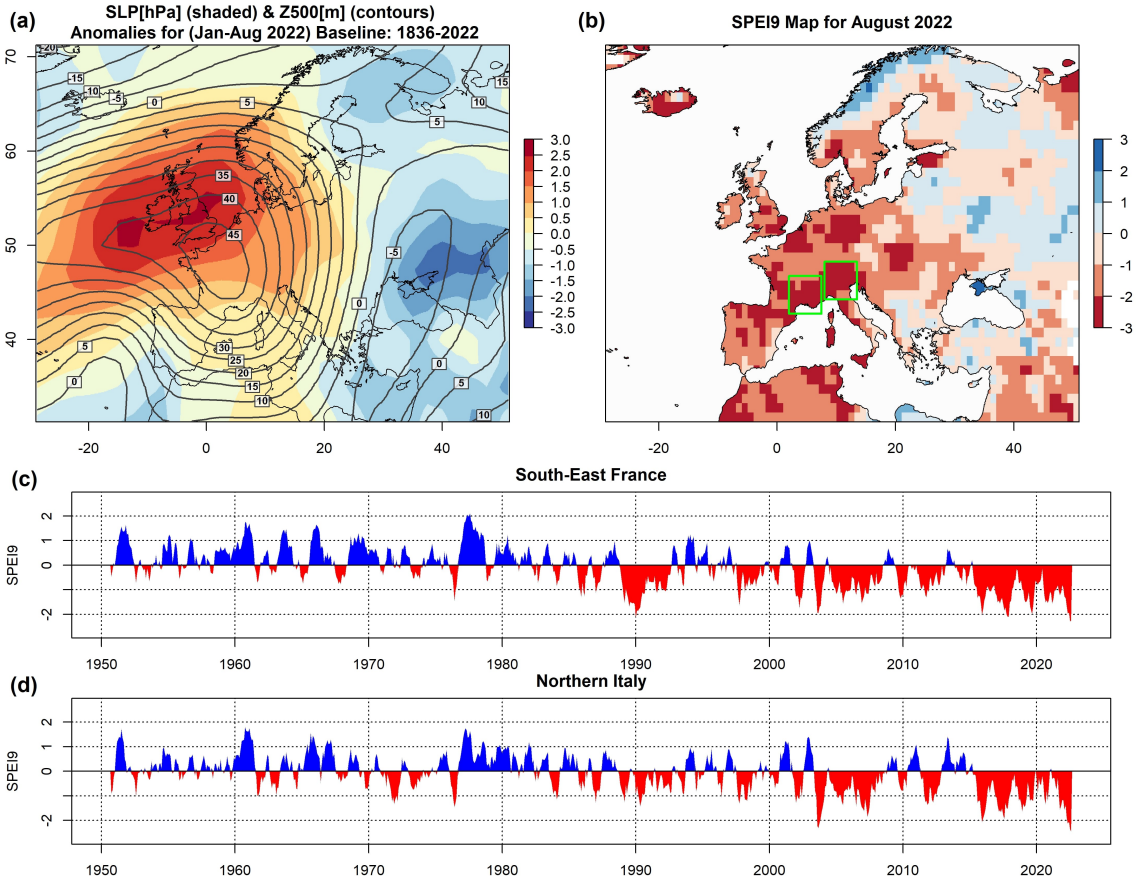

Figure 1. Characteristics of the 2022 European drought. (a) 2022 January-to-August anomalies of 500 hPa geopotential height (contour interval -15 and 45 m) and Mean Sea Level Pressure (shading interval -3 and 3 hPa), (b) map of SPEI9 in August 2022, and (c,d) SPEI9 time series obtained as an average of grid points within the selected regions highlighted in green.

Evapotranspiration. It has been demonstrated that high temperatures - typical of, e.g., heat waves - increase drought stress under precipitation shortages by dramatically increasing evapotranspiration [24]. The SPEI is calculated first by estimating the difference between precipitation and potential evapotranspiration at the surface, which provides a simple measure of the water deficit or surplus, and then aggregating it at different time scales (SPEI1, SPEI3, SPEI6,etc.). Similarly to the SPI, the time scale of accumulation of the water deficits (e.g., 3 months, 6 months, 12 months, etc.) is very important for practical reasons, as it differentiates meteorological droughts - typically of a few months' duration - from hydrological droughts, emerging at longer timescales (6 months or longer).

The large scale atmospheric circulation over the North Atlantic-European sector is investigated through the 500 hPa geopotential height (Z500) and sea level pressure (SLP). All Z500 and SLP data used in the analyses of the analogs of circulation (see

Sect. 2.3) are first detrended and then deseasonalized by subtracting, for each month, the 1836-2022 monthly average. Details on these applied procedures can be found in the Supplementary Material and in Fig. S2. For the circulation analogs defined through Z500 and SLP, we also monitor the corresponding 2-meter temperature, precipitation and SPEI9. We use the 2-meter temperature to keep track of the impact of global warming, and the precipitation rate and SPEI9 to further cross-check drought conditions. We do not apply any preprocessing to 2-meter temperature, the precipitation rate, and SPEI9. A list of the variables and their symbols, used in this study are shown in Table S1.

2.2. Data

In order to characterize the 2022 drought event over Europe (Fig. 1) we use SPEI9 obtained from the SPEI Global Drought Monitor, freely available at `https://spei.csic.es/index.html` at 1°×1° horizontal resolution from 1950 to present. The SPEI Global Drought Monitor offers near real-time SPEI estimates at various temporal scales (SPEI1, SPEI3, etc.) at the global scale, based on the NOAA NCEP CPC GHCN_CAMS gridded dataset for mean temperature and the Global Precipitation Climatology Centre for the monthly precipitation data.

To search for analogs of the 2022 atmospheric circulation over the North Atlantic-European sector, and their relationship to the drought, we use the NOAA-CIRES-DOE Twentieth Century Reanalysis, version 3 (20CRv3) [25]. 20CRv3 is the latest version of 20CR, and implements many substantial improvements relative to previous versions [26]. 20CRv3 reanalyses are created by assimilating only surface pressure values and using observed monthly sea ice and sea surface temperature distributions as boundary conditions. Estimates of the uncertainty are obtained using 80 ensemble members, which is a peculiar characteristic of 20CRv3. The choice of 20CRv3 - which spans the period 1836-2015 and it is available at 1°×1° horizontal resolution - is dictated by the need of having a century-long reanalysis product that can thus provide more reliable statistics with regards to rare events, as in the case of intense droughts, and a sufficient number of analogs of the atmospheric circulation anomaly associated with the 2022 drought. In order to cover the most recent years (i.e., 2016-2022), we complement 20CRv3 for the period January 2016-August 2022 with NCEP reanalysis [27]. We use both the NCEP/DOE and NCEP/NCAR reanalyses (Table S1). 20CRv3 and NCEP Reanalysis data are freely available at `https://psl.noaa.gov/data/gridded`. In order to eliminate differences between 20CRv3 and NCEP reanalysis datasets, we applied a bias correction to the complementary period 2016-2022 where datasets are obtained from NCEP reanalysis. Details of how we combined the two datasets as well as how bias corrections are performed are provided in the Supplementary Material and in Fig. S3. SPEI9 is calculated for the combined reanalyses 20CRv3 and NCEP by using the R package SPEI9 [5]. This tool assumes a log-logistic probability distribution [4] calibrated for 20CRv3 using all available years. We used the Thornthwaite equation as the method for determining potential evapotranspiration to be consistent with observations (SPEI

Global Drought Monitor).

We evaluate the effect of interannual and interdecadal variability on the 2022 drought and on past analog droughts using the Niño3.4 index for ENSO (1870 -present) and the Atlantic Multidecadal Oscillation (AMO, 1850 - present) monthly indices computed from the HadISST1 data – the same SST used in the 20CRv3 reanalysis – and retrieved from KNMI's climate explorer `www.climexp.knmi.nl`. Missing values are replaced by NaN and not counted in the analysis. We remark that NaN values represent only less or at most about 10% of the total data. In particular, the Niño3.4 index is as defined by [28] and the AMO index is computed as described in [29].

2.3. Analogs attribution method

The attribution method we use here is described in detail in [18], where it has been applied and validated for daily SLP maps associated with a number of extreme events occurred in 2021. In this study, we modify this method, born to deal with extreme events of the duration of a few days, in order to apply it to slow-evolving extreme events like droughts, which can have a duration of several months. To isolate the slow-evolving component of the atmospheric circulation (Fig.1a) and for consistency with SPEI9, we smooth Z500 and SLP by applying a nine-month backward moving average. We then search for analogs of the SLP and Z500 anomalies observed in August 2022 (Fig. 1a) in the factual period 1941-2021 and compare them to the analogs in the counterfactual period 1836-1915. The choice of these two periods is motivated by the need of having sufficiently long samples to select good analogs, while keeping a separation between periods with low and high CO2 emissions. For each period, we examine all monthly averaged maps and select the best 29 analogs, i.e. the maps minimizing the Euclidean distance to the event map itself. The number of 29 corresponds approximately to the smallest 3‰ Euclidean distances in each subset of our data. We tested the extraction of 15 to 30 analogous maps, without finding qualitatively important differences in our results. For the factual period, as is customary in attribution studies, the event itself is suppressed. In addition, we prohibit the search for analogs in 2022.

Unlike attribution techniques based on a statistical analysis of meteorological variables, conditioning to specific atmospheric circulation patterns via analogs allows us to link attribution to the dynamics driving extreme events. In addition, the analogs method allows us to determine when a weather event is unprecedented because of an atmospheric circulation that has never been observed in the past, making it statistically impossible to say whether climate change has made the event more likely. To account for the possible influence of low-frequency modes of natural variability in explaining the differences between the two periods, we also consider the possible roles of ENSO and AMO.

Following [18], we introduce additional indicators that further support our interpretation of analog-based results (see detailed description in Supplemental Material Section 3):

2.3.1. Analog quality Q. Q is the average Euclidean distance of a given circulation pattern from its closest 33 analogs. One can then compare Q associated with the extreme event to Q for each analog of the extreme event. If the value of Q for the extreme event belongs to the same distribution of the values of Q for the analogs, then the extreme event has good analogs. If instead the Q for the extreme event is larger than that of the analogs, then the extreme event is associated with a very unusual circulation pattern, and care must be taken in interpreting the results. Differences between the counterfactual and factual periods in the value of Q associated with the extreme event indicate whether the atmosphere is visiting states (analogs) that are more or less similar to the map associated with the extreme.

2.3.2. Predictability Index D. Using dynamical systems theory [30, 31, 32], we can compute the local dimension D of each Z500 (SLP) map [33, 34]. The local dimension is a proxy for the number of degrees of freedom of the field, meaning that the higher D, the more unpredictable the temporal evolution of the Z500 (SLP) maps will be [35, 36, 37]. If the dimension D of the extreme event analyzed is higher or lower than that of its analogs, then the extreme will be respectively less or more predictable than the closest dynamical situations identified in the data.

2.3.3. Persistence index Θ. Another quantity derived from dynamical systems theory is the persistence Θ of a given configuration [38]. Persistence estimates the number of subsequent months we are likely to observe a map that is an analog of the one under consideration.

2.3.4. Seasonality of analogs. We can count the number of analogs per each month to detect whether there has been a shift in circulation to months earlier or later in the season. This can have strong thermodynamic implications, for example, if a circulation leading to large positive temperature anomalies in early spring becomes more frequent later in the season when average temperatures are much higher.

We compute the analog quality, the predictability index and the persistence index, and their statistical distribution, for extreme events in the factual and counterfactual world. Similarly, we estimate the persistence of the analogs for the two periods.

2.4. Association with ENSO and AMO

To account for the effect of natural interannual and interdecadal variability, we extract from the entire time series of the ENSO and AMO indices only the values in correspondence of "analog" months, for both the counterfactual and factual periods. If the two distributions – ENSO (AMO) during analogs in the counterfactual period and ENSO (AMO) during analogs in the factual period – do differ significantly, then it is not possible to exclude that thermodynamic or dynamic differences in the analogs are partly due to these modes of natural variability, rather than anthropogenic forcing. On

the other hand, if it is not possible to reject the null hypothesis of equal distributions, observed changes in analogs cannot be due to these two modes of natural variability and hence are attributed to human activity. It is worth noting that such null hypothesis of no influence of natural variability is coherent with the view of [39].

To assess the significance of changes in factual vs. counterfactual distributions, we conduct in all cases a two-sided Cramér-von Mises test at the 0.05 significance level. If the p-value is smaller than 0.05, the null hypothesis ($H = 0$) that the two samples come from the same distribution can be rejected [40].

3. Results

We perform the analogs attribution on both Z500 and SLP. Our results do not sensibly depend on the choice of the variable nor on the choice of applying or not the bias corrections to the reanalyses products (see Supplementary). Here we present the results for Z500 20CRv3 and DOE data with bias corrections, referring the reader for all other cases to the Supplementary Material.

3.1. Pattern analysis

Figure 2a shows the Z500 anomaly field averaged over the time period December 2021-August 2022. We note a dipolar structure of the Z500 anomaly, with positive values on Western Europe and negative on Eastern Europe, typical of Atlantic ridge patterns [41]. Analogs for the counterfactual (Fig. 2b) and factual (Fig. 2c) periods show a similar dipolar structure. The difference between the analogs of the factual and counterfactual period, ΔZ500, highlights statistically significant diversities between the two fields (Fig. 2d). In particular, the factual climate features a dipole structure with larger positive anomalies over western Europe relative to the counterfactual climate. Furthermore, the positive anomaly has a larger spatial extension and it extends further westward over the Atlantic and southeastward towards the Mediterranean basin. This feature is pretty robust and independent of the choice of variables (SLP vs. Z500) and reanalyses (Fig. S4-Fig. S10).

Fig. 2e shows T2M averaged over December 2021-August 2022 while Fig. 2f-g show the average T2M associated with the two sets of analogs. The analysis for T2M shows that the temperature field of the 2022 drought (Fig. 2e) is exceptionally warmer when compared to those associated with analogs of the counterfactual (Fig. 2f) or factual (Fig. 2g) periods. The difference ΔT2M between the two is shown in (Fig. 2h) and it shows an impressing warming associated with the Z500 analogs in the factual periods, as we would somewhat expect due to the ongoing global warming [42]. Note that this warming is way beyond the average global (1.2°C) but also regional warming and does not include the event itself.

When comparing PRATE for the drought 2022 (Fig. 2i) with those associated with counterfactual (Fig. 2j) and factual (Fig. 2k) analogs, we note some similarities

such as large precipitation amounts over the Alps, Norway, and southern Iceland, while the western Atlantic is dryer in 2022 than in the analogs. Let us bear in mind that these are precipitation estimates obtained from a reanalysis and therefore do not have to be considered as reliable as real observations. While not accurate, they are still useful to connect circulation and thermal anomalies to precipitation deficits and hence droughts. What is more informative is the difference in PRATE associated with factual and counterfactual analogs (Fig. 2l), which shows a tendency to drier conditions in the factual climate relative to the counterfactual climate, with two minima over the British isles and over the Mediterranean.

We complete this analysis by comparing the pattern of SPEI9 of August 2022 (Fig. 2m; see also Fig. 1b for an estimate of the same field based on observations) with the typical SPEI9 patterns associated with the Z500 factual and counterfactual analogs (Fig. 2n-Fig. 2o). When comparing the structure of SPEI9 from counterfactual to factual period (Fig. 2p), we see an extension of the area with negative values from Eastern Atlantic and the Iberian peninsula to all Western and Southern Europe. In fact, the resulting difference ΔSPEI9 shows a marked tendency to negative values over all Europe. As SPEI9 takes into account both precipitation and surface potential evapotranspiration – which is temperature dependent – this patterns is fully consistent with both the tendency towards higher temperatures (Fig. 2h) and reduced precipitation (Fig. 2l) of Z500 analogs in the factual climate.

3.2. Dynamical indicators analysis

An analysis of the analogs quality Q (Fig. 2q) shows that factual analogs, as compared to counterfactual ones, are more similar to the Z500 pattern defined in Fig. 2a. This is because the Euclidean distance of the 2022 circulation pattern from the factual analogs (blue dots) is well centered with the distribution of the distances of 2022 analogs from their analogs (pink violin plot). Contrary to that, the distance of the 2022 circulation pattern from the counterfactual analogs is at the edge for the counterfactual (blue violin plot). The difference between the distribution of the quality for the two periods is significant with p-value virtually zero. However, this is not consistent through the different members of the 20CRv3 ensemble (see Section 3.5) so that these changes do not appear as robust.

The predictability (Fig. 2r) and the persistence (Fig. 2s) of the analogs do not show significant differences between the counterfactual and factual climates. The seasonality of the analogs (Fig. 2t) shows a tendency of observing such Z500 anomalies more in the summer and early autumn months in the factual period than in the counterfactual period. Supplementary Fig. S4-S10 show that this analysis is overall fairly qualitative insensitive to the choice of the variable (Z500 or SLP) or the dataset or the bias-correction procedure employed, with the exception of the persistence of the analogs, which show a tendency to be more common in winter and spring in the factual climate when SLP is employed.

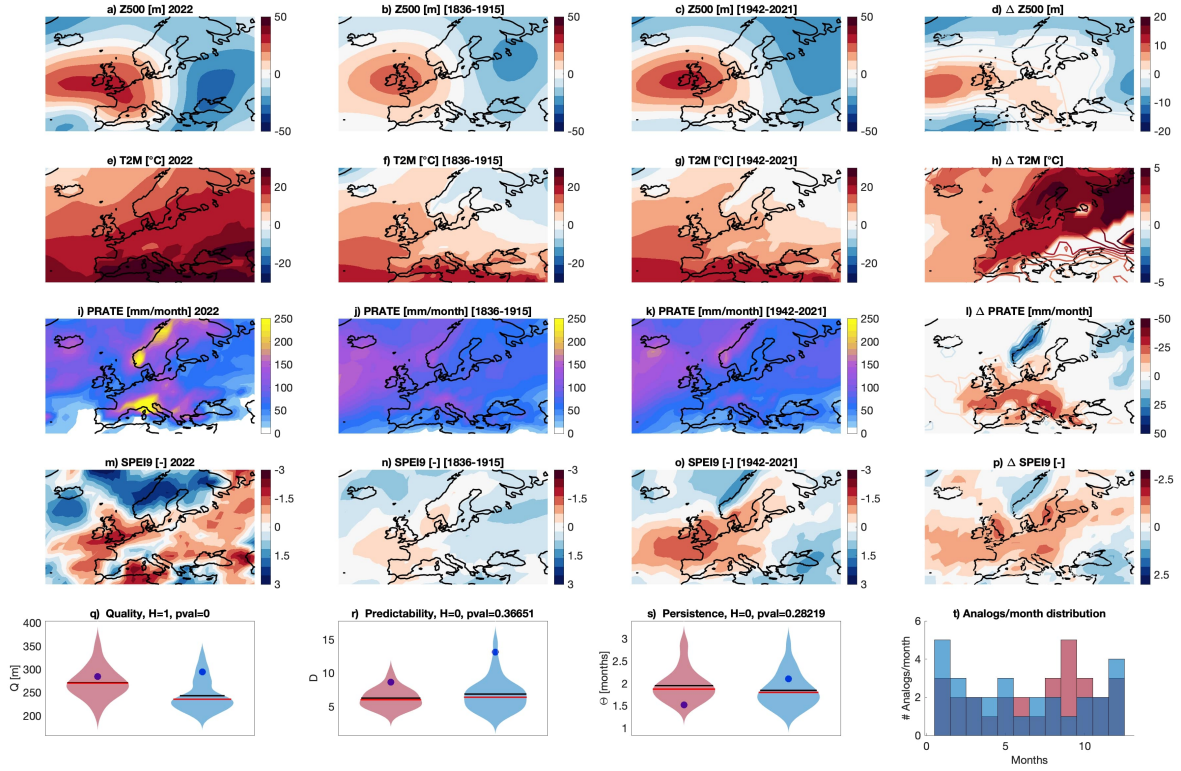

Figure 2. Attribution results for the 2022 Drought via analogs. December 2021 to August 2022 averaged mean 500 hPa geopotential height field Z500 (a), 2-meter temperatures T2M (e), monthly precipitation rate PRATE (i), SPEI9 index (m). Average of the 29 Z500 analogs found for the counterfactual [1836-1915] (b) and factual [1941-2021] (c) periods and corresponding 2-meter temperatures (f,g), daily precipitation rate (j,k) and SPEI9 (n,o). ΔZ500 (d), ΔT2M (h), Δ PRATE (i) and ΔSPEI9 (p) between factual and counterfactual periods: colored-filled areas show significant anomalies with respect to the bootstrap procedure. Violin plots for counterfactual (blue) and factual (orange) periods for the analogs Quality Q (q) the Predictability index D (r), the Persistence index Θ (s) and the distribution of analogs in each month (t). Black (red) lines in violin plots indicate mean (median) values. Titles in violin plots report the results H of the two-sided Cramér-von Mises test at the 0.05 significance level with the corresponding p-values (see section 2.4 for details).

3.3. Frequency of occurrence

In order to determine whether the atmospheric circulation that led to the 2022 drought (Fig. 1a, Fig. 2a) has become more frequent in the factual climate, we now examine whether there is a trend in the frequency of the associated analogs over the whole 1836-2021 period, again leaving the year 2022 outside of this search. This analysis will allow us to isolate circulation trends on top of that induced by the thermodynamics, as we are using detrended SLP and Z500 data. For this analysis, we set the quantile for the analogs search to 0.95, i.e. we consider the 5% closest analogs to the event, to have enough analogs in each decade to estimate a robust trend. We have however tested trends obtained for higher quantiles $(0.97, 0.98)$, i.e. looking at the 3% and 2% closest

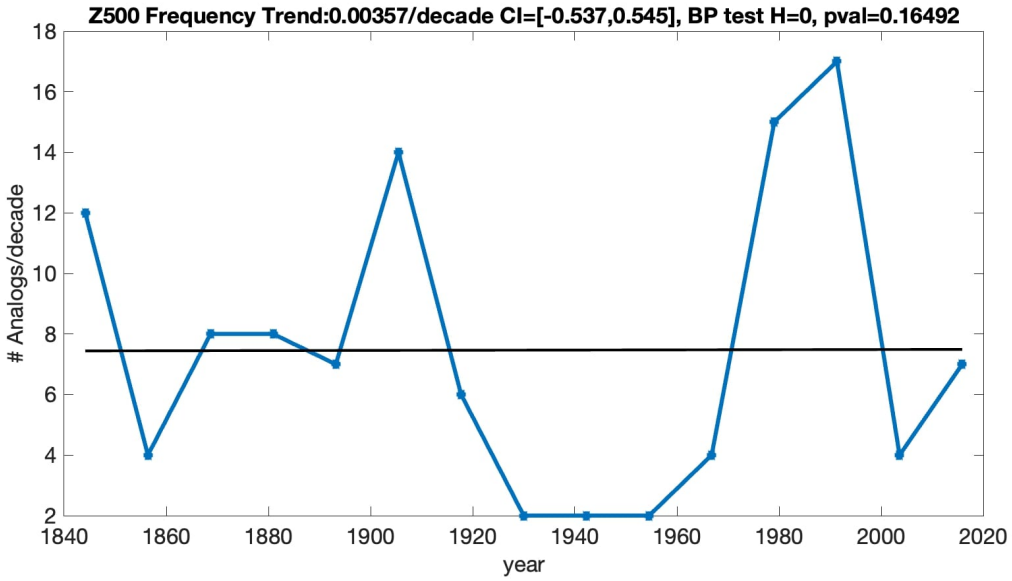

Figure 3. Evolution of the Frequency of analogs per decade. Evolution of the number of analogs per decade. In this case, analogs are computed for all the period 1836-2021. A linear fit is performed. The title reports the magnitude of the trends, the 95% confidence intervals (CI) of the a parameter for the fit computed using the Wald method [43] and the results H of the Breusch Pagan test [44] for the variability of analogs with its p-value

analogs without finding qualitative differences. Results are shown in Figure 3, where we can see the number of analogs per decade. We estimate a linear trend $ax + b$ where x is the number of analogs per decade and the upper and lower 95% confidence intervals (CI) of the a parameter of the fit using the Wald method [43]. The analysis shows an increasing variability in the frequency of the analogs without any significant increasing or decreasing trends. Similar results are obtained for SLP and other datasets (Fig. S11-S17). This leads us to conclude that the slow-evolving component of the circulation anomaly that drove the 2022 drought has not become more frequent in recent decades. Once the linear trend is removed, we investigate possible changes in the variability of the number of analogs using the Breusch-Pagan test [44] with a significance level 0.05. If the test statistic is found to be significant (H=1, pvalue < 0.05), it suggests that the residuals are not homoscedastic: in our case, this would mean that the analogs' variability changes over time. We tested this hypothesis in our datasets: for the Z500 variables H=0 in all cases (Figures S11-S13) and for all the 80 ensemble members (Table S2). For SLP only 15 members of the ensemble and the combination SLP bias corrected DOE (Figure S14) is compatible with a change of variability in time.

3.4. Dependence on ENSO and AMO

Finally, we examine the association of the analogs with two major modes of interannual and interdecadal variability, namely ENSO and AMO. We build the probability

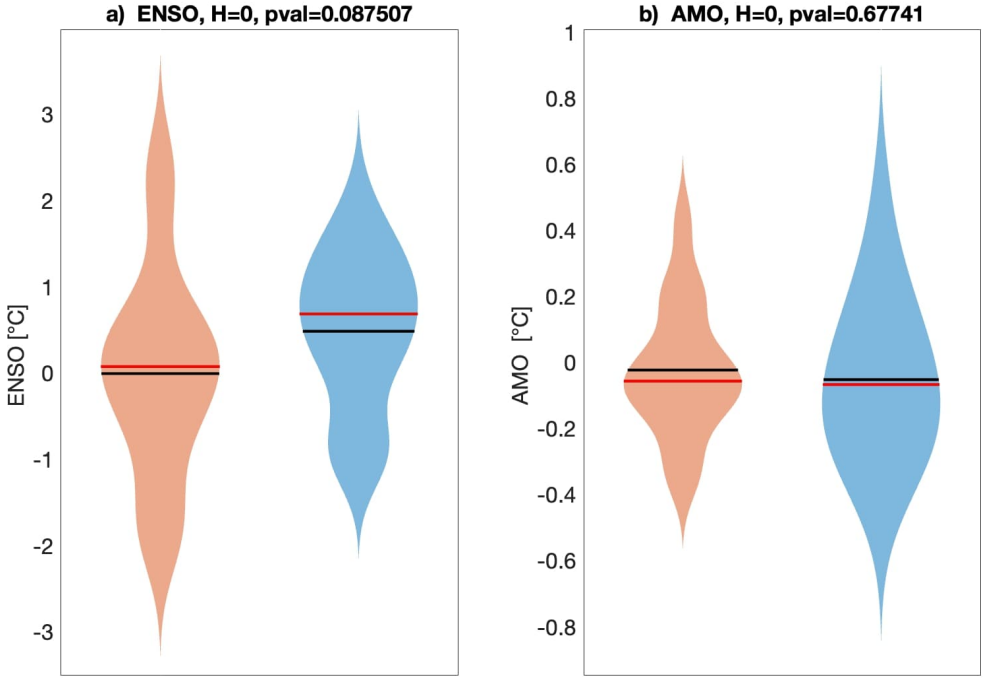

Figure 4. Analysis of the interannual and interdecadal variability. Violin plots for counterfactual (blue) and factual (orange) periods for ENSO (a) and AMO (b) values corresponding to the analogs months. Black (red) lines in violin plots indicate mean (median) values. Titles in violin plots report the results H of the two-sided Cramér-von Mises test at the 0.05 significance level with the corresponding p-values (see section 2.4 for details).

distributions of the values of the ENSO and AMO indices selected at the months of the occurrence of analogs. If there exists a strong association between ENSO or AMO, and the circulation anomaly of Fig. 2a, then we would find a probability distribution not centered around zero.

The results are shown in Fig. 4a for ENSO and in Fig. 4b for AMO. For the dataset used in the main text (20CRv3 plus NCEP/DOE) the analysis shows: (1) no significant changes in the distribution of ENSO (AMO) between the counterfactual and factual world, and (2) no tendency for El Niño or La Niña (positive AMO or negative AMO) to prevail during periods characterized by circulation analogs of the one seen during December 2021-August 2022. That would seem to reinforce our initial conjecture (Sect. 1) of no strong association between La Niña and the 2022 drought.

We note however that the p-value of the test for ENSO is equal to 0.088, close to the significance value of 0.05. Indeed some of the supplementary datasets shown in Fig. S18, S20, S21 show a significant change in the distribution of ENSO between the counterfactual and factual climate. Hence, we cannot completely reject a moderate role of interannual variability in exacerbating the 2022 drought. Interestingly, the same

analysis performed for the sea-level pressure patterns (Figs. S22-S24) show instead a dependence on the AMO but not on the ENSO.

3.5. Single-member analyses

The use of 20CRv3 reanalysis ensemble average at the beginning of the period can be problematic because it is based on a limited amount of observational data. This can lead to inaccuracies and biases in the ensemble average, which can affect the overall analysis. To address this issue, we repeated our analysis for all the 80 ensemble members. Results are reported in Supplemental Material Section 4, Figures S25-S28 and Table S2. This allows for a more comprehensive and accurate assessment of the data, as it takes into account the variability among the individual members. Results obtained for single members are largely consistent with those presented here for the ensemble means. The analysis of S25-S28 suggest that the standard deviation of the ensemble is way smaller than the averages, therefore the uncertainty in the reanalyses does not affect sensibly the results. Table S2 suggests that dynamical changes in predictability and persistence are more robust for SLP than Z500, and a prominent role of the AMO as sources of interdecadal variability. Only few members show changes in Analogs Quality, so that the results found in Figs. 2,S4-S10 (q) are specific of ensemble averages. For Predictability, Persistence and Variability, results of the ensemble are coherent with those of the ensemble means supporting our claim that analogs of our event have overall not changed significantly in time.

4. Discussion

We find a prominent role of the atmospheric circulation in driving the 2022 drought. There is a strong correspondence between the areas where Z500 was higher in the 2022 and the anomaly of this quantity in the factual vs counterfactual period. In particular, the geopotential height is not just higher but the area with positive anomalies is also larger. As a consequence, while in the counterfactual periods droughts associated with these synoptic situations were confined to the British Isles, France, and partially the Iberian peninsula, in the factual world they embrace a larger portion of continental Europe and Italy. There is therefore a sort of "inflating balloon" effect which expands the spatial extent of the drought and makes the anticyclonic dome higher, thus contributing to increasing the severity of the 2022 drought. This might be a "thermodynamic" effect of global warming [45]. In addition to that, we also found that factual analogs get "warmer", i.e., the near-surface temperature associated with them becomes higher (Fig. 2h). That leads to a more negative value of SPEI even if PRATE remains unchanged because higher surface temperature increases evapotranspiration, which dries the soil. This result is in line with [3], which focused on the exceptionality of the June-August soil moisture deficit in Europe and found that human-induced climate change made the 2022 root zone soil moisture drought about 3-4 times more likely, and the

surface soil moisture drought about 5-6 times more likely.

While the "balloon" expansion effect of Z500 is the most visible, we also note a change in the shape of the anticyclonic structure going from the counterfactual and factual periods, with the positive Z500 anomaly featuring a "crescent" shape from the Atlantic through Central Europe into the Mediterranean (Fig. 2d). While this change in shape is of dynamical nature and thus related to systematic changes in the atmospheric circulation goes beyond the scope of this study, but would deserve further attention in future studies.

No trends in the frequency of this pattern have been observed and we do not have enough elements pointing to a change in the variability of the analogs with time. Finally, the analysis of the interannual and interdecadal oceanic variability on the 2022 drought suggests that we cannot completely rule out the influence of ENSO for the upper-level circulation and for the Atlantic Multi-decadal Oscillation for the lower-level circulation, although such influences are likely to be very modest.

5. Conclusions

According to the World Meteorological Organization, drought represents one of the most damaging and life-threatening climate-related hazards [46]. The attribution of drought events to human-caused climate change is not as clear as for other types of weather hazards like, e.g., heatwaves, because of the confounding role of natural variability [19]. Exceptional droughts have in fact occurred over the last two thousand years in association with decadal variations in sea surface temperatures [47]. While the last IPCC 6th Assessment Report states that we have "medium confidence" in attributing to human-induced climate change the increases in agricultural and ecological droughts because of increased land evapotranspiration [48, 42, 49], attribution to human-caused climate change of meteorological droughts – directly related to rainfall deficits and hence to atmospheric dynamics – remains challenging. Nevertheless, progress has been made and recent research highlighted the role of global warming in the exacerbation of some recent extraordinary meteorological droughts [50, 51, 20, 21].

In this study we considered the 2022 European-Mediterranean drought [1, 2] and investigated the exceptionality of the event and of its atmospheric drivers in a century-long reanalysis (1836-2021) using the analog-based methodology proposed in [18]. Our results indicate a role for ACC in making the atmospheric anticyclonic anomaly "stronger" and "warmer", two facts that in turn caused more widespread and exacerbated drought conditions. Conversely, we found that the frequency of occurrence of such a slow-evolving circulation component has not significantly changed over the last two centuries. These conclusions highlight a thermodynamic component in the exacerbation of droughts by human-caused global warming, while no strong evidence was found about a dynamical component - i.e., a change in circulation – in the recent period which could have triggered the 2022 drought.

While our study heavily relies on the observational datasets used and does not

employ climate models, our results appear robust to the choice of meteorological variables and reanalysis. They further illustrate the capability of a reanalysis-based attribution conditioned on the atmospheric circulation on longer time-scales suggesting that this methodology could also be used to investigate other long-lasting events driven by synoptic situations such as prolonged cold periods or heatwaves.

An approach based only on atmospheric reanalysis, like the one applied in this study, while providing important information on the likelihood of the 2022 drought, has some limitations for attributing this extreme event to human-caused climate change, that is, first, the impossibility to define a counterfactual climate with no anthropogenic forcing and, second, the limited number of years available in reanalyses datasets. In a follow-up study thus we plan to complement this study by applying this method to climate models too, and in particular to single model initial-condition large ensembles [52, 53, 54, 20, 55]. While these models are affected by systematic biases which can compromise their realism, they allow for a more rigorous definition of factual and counterfactual climate, and provide thousands of years of data is available for more robust statistics.

Acknowledgments

D. F. received support from the European Union's Horizon 2020 research and innovation programme under grant agreement No. 101003469 (XAIDA) and the Marie Sklodowska-Curie grant agreement No. 956396 (EDIPI).

Author Contributions

S.P. devised the study, D.F. performed the analyses and B.B. prepared the datasets and performed the bias corrections. All authors contributed to discussing and writing the paper.

Competing Interest

The authors declare no competing interests nor conflicts of interest. No human or animal data have been used in this study.

Data Availability

The data that support the findings of this study are available upon request from the authors. In addition, all other input data (SLP, Z500, T2M, and PRATE), climate indices (ENSO and AMO), and observed drought index (SPEI9) used in this study are publicly available at https://psl.noaa.gov/data/gridded/, https://climexp.knmi.nl, and https://spei.csic.es/map/, respectively.

References

[1] Toreti A, Bavera D, Avanzi F, Cammalleri C, De Felice M, de Jager A, Di Ciollo C, Gabellani S, Maetens W, Magni D, Manfron G, Masante D, Mazzeschi M, McCormick N, Naumann G, Niemeyer S, Rossi L, Seguini L, Spinoni J and van den Berg M 2022 JRC128974

[2] Toreti A, Bavera D, Acosta Navarro J, Cammalleri C, de Jager A, Di Ciollo C, Hrast Essenfelder A, Maetens W, Magni D, Masante D, Mazzeschi M, Niemeyer S and Spinoni J 2022 *Publications Office of the European Union, Luxembourg* JRC130493

[3] Schumacher D L, Zachariah M, Otto F, Barnes C, Philip S, Kew S, Vahlberg M, Singh R, Heinrich D, Arrighi J, van Aalst M, Thalheimer L, Raju1 E, Hauser M, Hirschi M, Gudmundsson L, Beaudoing H K, Rodell M, Li S, Yang W, Vecchi G A, Vautard R, Harrington L J and Seneviratne S I 2022 *WWA: World Weather Attribution*

[4] Vicente-Serrano S, Beguería S and I L J 2010 *J. Climate* **23** 1696–1718

[5] Beguería S, Vicente-Serrano S, Reig F and Latorre B 2014 *Int. J. Climatol.* **34** 3001–3023

[6] Baruth B, Bassu S, W B, Biavetti I, Bratu M, Cerrani I, Chemin Y, Claverie M, De Palma P, Fumagalli D, Manfron G, Morel J, Nisini L, Panarello L, Ronchetti G, Seguini L, Tarnavsky E, van den Berg M, Zajac Z and Zucchini A 2022 *JRC MARS Bulletin* **30** URL https://ec.europa.eu/jrc/en/mars/bulletins

[7] Mishra A K and Singh V P 2010 *J. Hydrol.* **391** 202–216

[8] Afshar M, Bulut B, Duzenli E, Amjad M and Yilmaz M 2022 *Agricultural and Forest Meteorology* **316** 108848

[9] Miralles D, Gentine P, Seneviratne S I and Teuling A J 2019 *Ann. N. Y. Acad. Sci.* **1436** 19–35

[10] Brönnimann S, Xoplaki E, Casty C, Pauling A and Luterbacher J 2007 *Clim. Dyn.* **28** 181–197

[11] Brönnimann S 2007 *Rev. Geophys.* **45** RG3003

[12] López-Parages J, Rodríguez-Fonseca B, Dommenget D and Frauen C 2016 *Clim. Dynamics* **47** 2071–2084

[13] Reuters 2022

[14] Bost A F, Villeneuve A, Armand M, Zabalza F, Gauchard Y, Foucart S and Rof G 2022 *Le Monde*

[15] Kaleem J and Johnson S 2022 *Los Angeles Times*

[16] Yiou P, Jézéquel A, Naveau P, Otto F E L, Vautard R and Vrac M 2017 *Adv. Stat. Clim. Meteorol. Oceanogr.* **3** 17–31

[17] Otto F E L 2017 *Annu. Rev. Environ. Resour.* **42** 627–646

[18] Faranda D, Bourdin S, Ginesta M, Krouma M, Noyelle R, Pons F, Yiou P and Messori G 2022 *Weather Clim. Dynam.* **3** 1311–1340

[19] NAS 2016 *Natl. Acad. Sci. Eng. Med.* 166pp

[20] Pascale S, Kapnick S and Delworth TLand Cooke W 2020 *Proceedings of the National Academy of Sciences of the United States of America* **117** 29495–29503

[21] Pascale S, Kapnick S, Delworth T, Hidalgo H and Cooke W 2021 *Climatic Change* **168** 1–21

[22] van der Wiel K, Lenderink G and de Vries H 2021 *Weather and Climate Extremes* **33** 100350 iSBN: 2212-0947 Publisher: Elsevier

[23] Hayes M, Wilhite D, Svoboda M and Vanyarkho 1999 *Bulletin of the American Meteorological Society* **80** 429–438

[24] Adams H, Guardiola-Claramonte M, Barron-Gafford G A, Villegas J C, Breshears D D, Zou C B, Troch P A and Huxman T E 2009 *Proceedings of the National Academy of Sciences of the United States of America* **106** 7063–7066

[25] Compo G P, Whitaker J S, Sardeshmukh P D, Matsui N, Allan R J, Yin X, Gleason B E, Vose R S, Rutledge G, Bessemoulin P *et al.* 2011 *Quarterly Journal of the Royal Meteorological Society* **137** 1–28

[26] Slivinski L C, Gilbert P C, Jeffrey S W, Sardeshmukh P D, Giese B S, McColl C, Allan R, Yin X, Vose R, Titchner H, Kennedy J, Spencer L J, Ashcroft L, Brönnimann S, Brunet M, Camuffo D, Cornes R, Cram T A, Crouthamel R, Domínguez-Castro F, Freeman J E, Gergis J, Hawkins E,

Jones P D, Jourdain S, Kaplan A, Kubota H, F L, Lee T C, Lorrey A, Luterbacher J, Maugeri M, Mock C J, Kent Moore G, Przybylak R, Pudmenzky C, Reason C, Slonosky V C, Smith C A, Tinz B, Trewin B, Valente M A, Wang X L, Wilkinson C, Wood K and Wyszynski P 2019 *Q. J. R. Meteorol. Soc.* **724** 2876–2908

[27] Kalnay E, Kanamitsu M, Kistler R, Collins W, Deaven D, Gandin L, Iredell M, Saha S, White G, Woollen J, Zhu Y, Chelliah M, Ebisuzaki W, Higgins W, Janowiak J, Mo K C, Ropelewski C, Wang J, Leetmaa A, Reynolds R, Jenne R and Joseph D 1996 *Bulletin of the American Meteorological Society* **77** 437–472 ISSN 0003-0007 URL https://doi.org/10.1175/1520-0477(1996)077<0437:TNYRP>2.0.CO;2

[28] Huang B, Thorne P W, Banzon V F, Boyer T, Chepurin G, Lawrimore J H, Menne M J, Smith T M, Vose R S and Zhang H M 2017 *Journal of Climate* **30** 8179–8205

[29] Trenberth K E and Shea D J 2006 *Geophysical research letters* **33**

[30] Freitas A C M, Freitas J M and Todd M 2011 *Journal of Statistical Physics* **142** 108–126

[31] Freitas A C M, Freitas J M and Vaienti S 2016 *arXiv preprint arXiv:1605.06287*

[32] Lucarini V, Faranda D, Freitas A C M, Freitas J M, Holland M, Kuna T, Nicol M, Todd M and Vaienti S 2016 *Extremes and recurrence in dynamical systems* (John Wiley & Sons) ISBN 1-118-63219-2

[33] Faranda D, Messori G and Yiou P 2017 *Scientific reports* **7** 41278 URL https://www.nature.com/articles/srep41278.pdf

[34] Faranda D, Messori G and Vannitsem S 2019 *Tellus A: Dynamic Meteorology and Oceanography* **71** 1–11

[35] Faranda D, Messori G and Yiou P 2017 *Scientific reports* **7** 41278

[36] Messori G, Caballero R and Faranda D 2017 *Geophysical Research Letters* **44** 3346–3354

[37] Hochman A, Alpert P, Harpaz T, Saaroni H and Messori G 2019 *Science advances* **5** eaau0936

[38] Faranda D, Vrac M, Yiou P, Jézéquel A and Thao S 2020 *Geophysical Research Letters* **47** e2020GL088002

[39] Trenberth K E 2011 *Wiley Interdisciplinary Reviews: Climate Change* **2** 925–930

[40] Anderson T W 1962 *The Annals of Mathematical Statistics* 1148–1159

[41] Dorrington J, Strommen K and Fabiano F 2022 *Weather and Climate Dynamics* **3** 505–533

[42] Allan R P, Hawkins E, Bellouin N and Collins B 2021

[43] Stein C and Wald A 1947 *The Annals of Mathematical Statistics* 427–433

[44] Breusch T S and Pagan A R 1980 *The review of economic studies* **47** 239–253

[45] Faranda D, Vrac M, Yiou P, Jézéquel A and Thao S 2020 *Geophys. Res. Lett.* **47** e2020GL088002 iSBN: 0094-8276 Publisher: Wiley Online Library

[46] World Meteorological Organization 2021 Weather-related disasters increase over past 50 years, causing more damage but fewer deaths URL https://public.wmo.int/en/media/press-release/weather-related-disasters-increase-over-past-50-years-causing-more-damage-fewer

[47] Cook B I, Smerdon J E, Cook E R, Park Williams A, Anchukaitis K J, Mankin J S, Allen K, Andreu-Hayles L, Ault T R, Belmecheri S, Coats S, Coulthard B, Fosu B, Grierson P, Griffin D, Herrera D A, a Ionita M, Lehner F, Leland C, Marvel K, Morales M S, Mishra V, Ngoma J, Nguyen H T T, O'Donnell A, Palmer J, Rao M P, Rodriguez-Caton M, Seager R, Stahle D W, Stevenson S, Thapa U K, Varuolo-Clarke A M and Wise E K 2022 *Nat. Rev. Earth Environ.* **3** 741–757

[48] Herrera D A, Ault T R, Fasullo J T, Coats S J, Carrillo C M, Cook B I and Williams A P 2018 *Geophysical Research Letters* **45** 10,619–10,626

[49] Seneviratne S, Zhang X, Adnan M, Badi W, Dereczynski C, Luca A D, Ghosh S, Iskandar I, Kossin J, Lewis S, Otto F, Pinto I, Satoh M, Vicente-Serrano S, Wehner M, and Zhou B 2021

[50] Fischer E M, Seneviratne S I, Lüthi D and Schär C 2007 *Geophysical Research Letters* **34**

[51] Otto F E L, Wolski P, Lehner F, Tebaldi C, van Oldenborgh G, Hogesteeger S, Singh R, Holden P, Fuckar N, Odoulami R and New M 2018 *Environ. Res. Lett.* **13** 124010

[52] Lehner F, Coats S, Stocker T F, Pendergrass A G, Sanderson B M, Raible C C, and Smerdon J E 2017 *Geophys. Res. Lett.* **44** 7419–7428
[53] Deser C, Lehner F, Rodgers K B, Ault T, Delworth T L, DiNezio P N, Fiore A, Frankignoul C, Fyfe J C and Horton D E 2020 *Nature Climate Change* 1–10 iSBN: 1758-6798 Publisher: Nature Publishing Group
[54] Zscheischler J and Fischer E M 2020 *Weather and Climate Extremes* **29** 100270
[55] Gessner C, Fischer E M, Beyerle U and Knutti R 2022 *Weather and Climate Extremes* **38** 100512

Supplemental Material for "Persistent anticyclonic conditions and climate change exacerbated the exceptional 2022 European-Mediterranean drought"

Davide Faranda[1,2,3,*], **Salvatore Pascale**[4,5,*], **Burak Bulut**[1,*]

[1] Laboratoire des Sciences du Climat et de l'Environnement, UMR 8212 CEA-CNRS-UVSQ, Université Paris-Saclay & IPSL, CE Saclay l'Orme des Merisiers, 91191, Gif-sur-Yvette, France

[2] London Mathematical Laboratory, 8 Margravine Gardens, London, W6 8RH, British Islands

[3] Laboratoire de Météorologie Dynamique/IPSL, École Normale Supérieure, PSL Research University, Sorbonne Université, École Polytechnique, IP Paris, CNRS, 75005, Paris, France

[4] University of Bologna, Department of Physics and Astronomy, 40126, Bologna, Italy

[5] Centre for Sustainability and Climate Change, Bologna Business School, 40136, Bologna, Italy

[*] All authors have equally contributed to this work

E-mail: `davide.faranda@cea.fr, salvatore.pascale@unibo.it, burak.bulut@cea.fr`

This Supplemental Material contains:

- Supplemental Text Sections 1-4
- Supplemental Tables S1-S2
- Supplemental Figures S1-S28

1. Anomalies calculation for the analog analysis

In this section, we provided information about how anomalies of SLP and Z500 were calculated for the analog analysis.

Firstly, the normalization of the datasets is achieved in two steps; firstly, the raw data (x) is purged from its linear trend (x'), and secondly, the seasonality effect is removed by discarding long-time (1836-2022) monthly averages from corresponding months (x"). Secondly, the moving average of each month (x"') is obtained by taking the mean of the values from the related month and 8 months prior (i.e., for August, months between January and August). The results of each applied step to obtain anomalies are shown in (Fig.S2).

2. Combining the 20CR and NCEP reanalyses and bias correction

In the following section, we describe why a bias correction is required before combining two reanalysis datasets and how we achieved the bias correction. In addition to the bias corrected datasets, we also provided merged datasets without using any correction.

It is required to merge two different datasets in order to provide uninterrupted data in the time period selected for the scope of the study. For this purpose, the 20CR dataset available between 01/1836 - 12/2015 and NCEP/DOE between 01/1979 - 08/2022 (and NCEP/NCAR 01/1948 - 08/2022) are combined. Firstly, all datasets are aggregated to the lowest resolution 2.5° using linear interpolation in order to eliminate the difference in spatial resolution. Then, it is necessary to eliminate the systematic difference between the two datasets, which has an effect on the calculation of the drought index. The linear rescaling method is used for the bias correction using the given equation below. The most linear relation between reference dataset X and the dataset to be rescaled Y is considered to implement the linear rescaling method in the form

$$Y^* = \mu_X + (Y - \mu_Y)c_Y \tag{1}$$

where Y^* is the rescaled version of Y, μ_X and μ_Y are time averages of X and Y, and c_Y is a scalar rescaling factor found by using variance-based linear methods as

$$c_Y = \sigma_X/\sigma_Y \tag{2}$$

where σ_X and σ_Y are standard deviations of X and Y datasets, respectively. Here in these equations, X and Y datasets refer to 20CR datasets and Reanalysis datasets within the commonly available period (01/1979 - 12/2015 for NCEP/DOE and 01/1948 - 12/2015 for NCEP/NCAR), respectively.

As a result, the datasets used in this study are obtained from the combination of all available raw 20CR datasets for the dates between 01/1836 - 12/2015, and either bias-corrected or not NCEP/DOE or NCEP/NCAR datasets for 01/2016 - 08/2022. The time series obtained with and without the bias correction method and the SPEI9 values, calculated from these two different time series are shown in (Fig.S3).

The Genova example showed that if we do not use bias correction when we merge two datasets and calculate SPEI9, it is not possible to catch drought events after 2016 due to the difference between the variables of the two datasets (Fig.S3 f). On the other hand, if we apply a linear rescaling method based on parameters obtained from the common years, we can calculate SPEI9 values (Fig.S3 g) consistent with the observed SPEI9 values obtained from SPEI Global Drought Monitor shown in the main text (Fig 1).

3. Detailed explanation of the Analogs Metrics

3.1. Predictability

The attractor of a dynamical system is a geometric object defined in the space hosting all the possible states of the system (phase-space). Each point ζ on the attractor can be characterized by two dynamical indicators: the local dimension D, which indicates the number of degrees of freedom active locally around ζ, and the persistence Θ, a measure of the mean residence time of the system around ζ [1]. To determine D, we exploit recent results from the application of extreme value theory to Poincaré recurrences in dynamical systems. This approach considers long trajectories of a system — in our case successions of monthly Z500 or SLP latitude–longitude maps — corresponding to a sequence of states on the attractor. For a given point ζ in phase space (e.g., a given Z500 or SLP map), we compute the probability that the system returns within a ball of radius ϵ centered on the point ζ. The [2] theorem, modified by [3], states that logarithmic returns:

$$g(x(t)) = -\log(\mathrm{dist}(x(t), \zeta)) \tag{3}$$

yield a probability distribution such that:

$$\Pr(z > s(q)) \simeq \exp\left[-\vartheta(\zeta)\left(\frac{z-\mu(\zeta)}{\sigma(\zeta)}\right)\right] \tag{4}$$

where $z = g(x(t))$ and s is a high threshold associated to a quantile q of the series $g(x(t))$. Requiring that the orbit falls within a ball of radius ϵ around the point ζ is equivalent to asking that the series $g(x(t))$ is over the threshold s; therefore, the ball radius ϵ is simply $e^{-s(q)}$. The resulting distribution is the exponential member of the Generalized Pareto Distribution family. The parameters μ and σ, namely the location and the scale parameter of the distribution, depend on the point ζ in phase space. $\mu(\zeta)$

corresponds to the threshold $s(q)$ while the local dimension $D(\zeta)$ can be obtained via the relation $\sigma = 1/D(\zeta)$. This is the metric of predictability introduced in the manuscript.

When $x(t)$ contains all the variables of the system, the estimation of D based on extreme value theory has a number of advantages over traditional methods (e.g. the box counting algorithm [4, 5]). First, it does not require to estimate the volume of different sets in scale-space: the selection of $s(q)$ based on the quantile provides a selection of different scales s which depends on the recurrence rate around the point ζ. Moreover, it does not require the a priori selection of the maximum embedding dimension as the observable g is always a univariate time-series.

3.2. Persistence

The persistence of the state ζ is measured via the extremal index $0 < \vartheta(\zeta) < 1$, an adimensional parameter, from which we extract $\Theta(\zeta) = \Delta t/\vartheta(\zeta)$. Here, Δt is the timestep of the dataset being analysed. $\Theta(\zeta)$ is therefore the average residence time of trajectories around ζ, namely the metric of persistence introduced in the manuscript, and it has unit of a time (in this study months). If ζ is a fixed point of the attractor, then $\Theta(\zeta) = \infty$. For a trajectory that leaves the neighborhood of ζ at the next time iteration, $\Theta = 1$. To estimate ϑ, we adopt the Süveges estimator [6]. For further details on the the extremal index, see [7].

3.3. Quality

Q is the average euclidean distance of a given month from its closest 29 analogs [8]. One can then compare Q for the targeted SLP or Z500 map to Q for each analogue of the target. If the value of Q for the targeted map belongs to the same distribution as, or is smaller than, the values of Q for the analogs, then the event has good analogs and attribution can be performed. If instead the Q for the targeted map is larger than that of the analogue months, then this indicates a highly unusual Z500 or SLP configuration and the results of the attribution analysis must be interpreted with care. Differences between the counterfactual and factual periods in the value of Q for the peak month of the targeted map indicate whether the the atmosphere is visiting states (analogs) that are more or less similar to the map associated with the extreme. Differences in the distribution of Q for the 29 analogs indicate whether those states are in turn becoming more or less "typical" of the atmospheric variability. In order to test the homogeneity of the analogs in the two periods, we have computed Q for all months in the factual and counterfactual periods on the wide North Atlantic domain and applied the two-sided Cramér-von Mises test at the 0.05 significance level. The analogs quality diagnostic provides information on the fact that we have enough good and independent analogs to perform the analysis for the following reasons: i) the distance of the targeted maps from the analogs (dark dots in Figures 1,S4-S10 (q)) is within the range of that of the analogs of the analogs. If we did not have good analogs the dots would lie outside of the violins for factual and counterfactual periods. ii) if the number of independent analogs for

study would not be sufficient, the violin plots in Figures 1,S4-S10 (q) would not show a continuous distribution probability density function but rather consist of discontinuous and discrete patches.

4. Analysis for each member of the 20CRv3 ensemble

The use of 20CRv3 reanalysis ensemble average at the beginning of the period can be problematic because it is based on a limited amount of observational data. This can lead to inaccuracies and biases in the ensemble average, which can affect the overall analysis. To address this issue, it is common practice to use individual members of the ensemble, rather than the ensemble average, for the analysis. This allows for a more comprehensive and accurate assessment of the data, as it takes into account the variability among the individual members. To ensure robustness of our results with respect to this issue, we have repeated the analysis for each of the 80 individual members of the 20CRv3. Figures S25-S28 and Table S2. Patterns show for Δ Z500 (Figure S25a), Δ SLP (Figure S26a) closely match those shown in Figure 1d and Figure S7d in shape and in magnitude of the structures. The same observation applies for the diagnostic T2M, PRATE and SPEI9 variables in the analyses. To get an idea of whether these results are significant with respect to the member variability, we display in Figures S27-S28, the standard deviations of the ensemble. The scale of the standard deviation for all variables but T2M is an order of magnitude smaller than that of the anomalies, proving the robustness of our analysis for circulation fields with respect to the 20CRv3 ensemble. For T2M, the uncertainty among members is mostly concentrated in Eastern Europe and Russia, i.e. regions that are not concerned by our analysis. Table S2 shows the number of ensemble members scoring H=1 in the statistical tests of Cramér-von Mises [9] and the Breusch-Pagan test for the Variability [10]. It allows to verify that there are not many members for which the analogs quality Q is different among factual and counterfactual periods. There is about half of the ensemble showing changes in Predictability and persistence for the SLP. Changes in the AMO for both of the SLP and Z500 are found in about half of the members, while very few ensemble members seem to point to a change in variability of the analogs with time.

Supplemental References

[1] Faranda D, Messori G and Yiou P 2017 *Scientific reports* **7** 41278
[2] Freitas A C M, Freitas J M and Todd M 2010 *Probability Theory and Related Fields* **147** 675–710
[3] Lucarini V, Faranda D and Wouters J 2012 *Journal of statistical physics* **147** 63–73
[4] Liebovitch L S and Toth T 1989 *physics Letters A* **141** 386–390
[5] Sarkar N and Chaudhuri B B 1994 *IEEE Transactions on systems, man, and cybernetics* **24** 115–120
[6] Süveges M 2007 *Extremes* **10** 41–55
[7] Moloney N R, Faranda D and Sato Y 2019 *Chaos: An Interdisciplinary Journal of Nonlinear Science* **29** 022101

[8] Faranda D, Vrac M, Yiou P, Jézéquel A and Thao S 2020 *Geophys. Res. Lett.* **47** e2020GL088002 iSBN: 0094-8276 Publisher: Wiley Online Library
[9] Anderson T W 1962 *The Annals of Mathematical Statistics* 1148–1159
[10] Breusch T S and Pagan A R 1980 *The review of economic studies* **47** 239–253

5. Supplemental Tables and Figures

Variable	Spatial Resolution	Temporal Coverage	Reference
SLP, Z500, PRATE, T2M, SPEI9	1° x 1°	01/1836-12/2015	NOAA/CIRES/DOE 20CRv3, (Slivinsk et al., 2019)
SLP, Z500	2.5° x 2.5°	01/1948-08/2022	NCEP/NCAR Reanalysis I, (Kalnay et al., 1996)
PRATE, T2M	1.875° x 1.90°	01/1979-08/2022	NCEP/DOE Reanalysis II, (Kanamitsu et al., 2002)
ENSO	1° x 1°	01/1870-08/2022	HadISST1 Nino3.4 Index, (Rayner et al., 2003)
AMO	1° x 1°	01/1850-08/2022	Atlantic Multidecadal Variability index, (van Oldenborgh et al., 2009)
SPEI9	1° x 1°	01/1950-08/2022	SPEI9Global Drought Monitor, (Beguería et al., 2014)

Table S1. Data sets used in the study, the period of record available, spatial resolution, and references.

Test on Analogs Metrics	# with H=1 (Z500)	# with H=1 (SLP)
Cramér-von Mises for Quality Q	23	5
Cramér-von Mises for Predictability D	22	53
Cramér-von Mises for Persistence Θ	7	36
Cramér-von Mises for AMO	49	34
Cramér-von Mises for ENSO	4	2
Breusch-Pagan for Variability	0	15

Table S2. Number of ensemble members scoring H=1 in the statistical tests of Cramér-von Mises and the Breusch-Pagan test for the Variability.

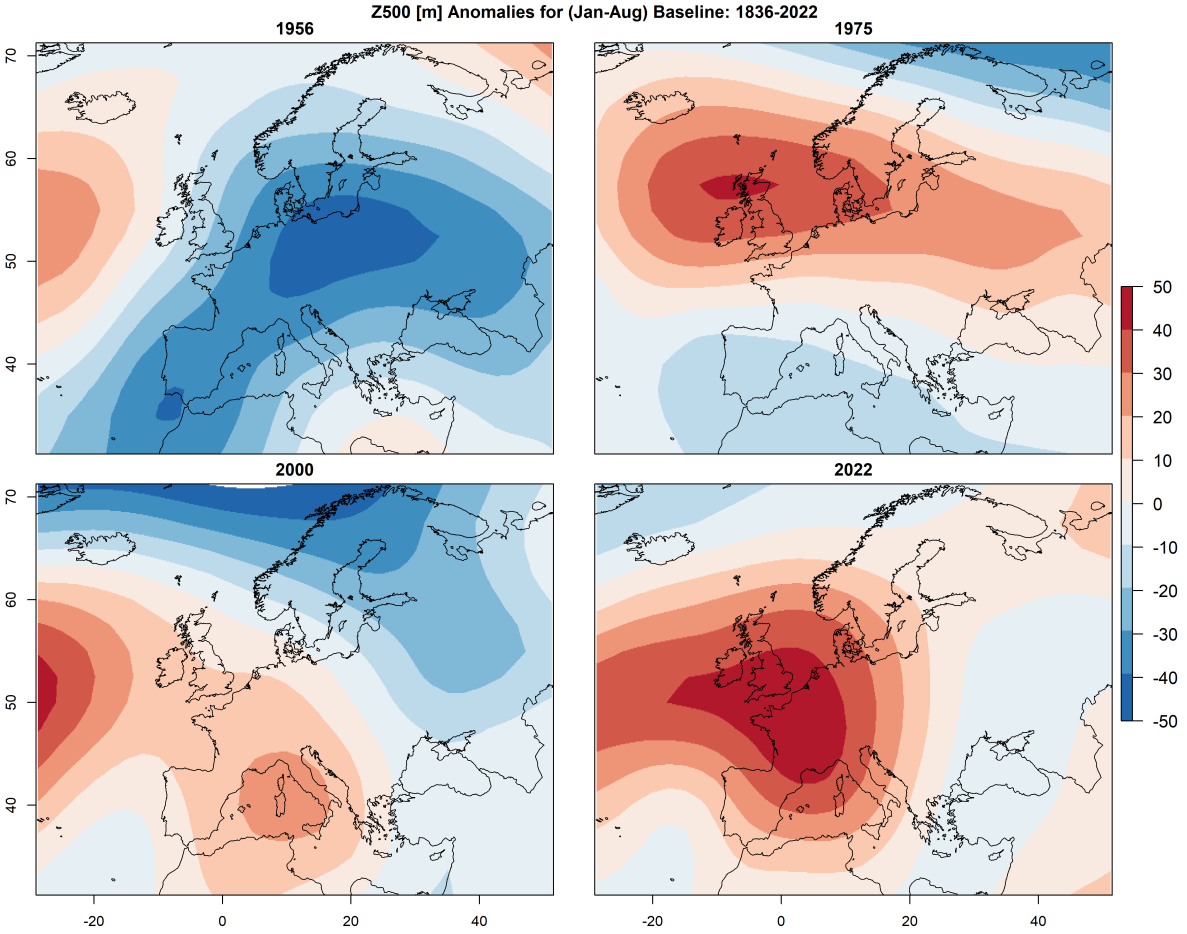

Figure S1. Circulation anomalies during persisting 3-year La Niña. 500 hPa January-to-August mean geopotential height anomaly in years (i.e., 1956, 1975, 2000, 2022) characterized by a three-year persisting La Niña.

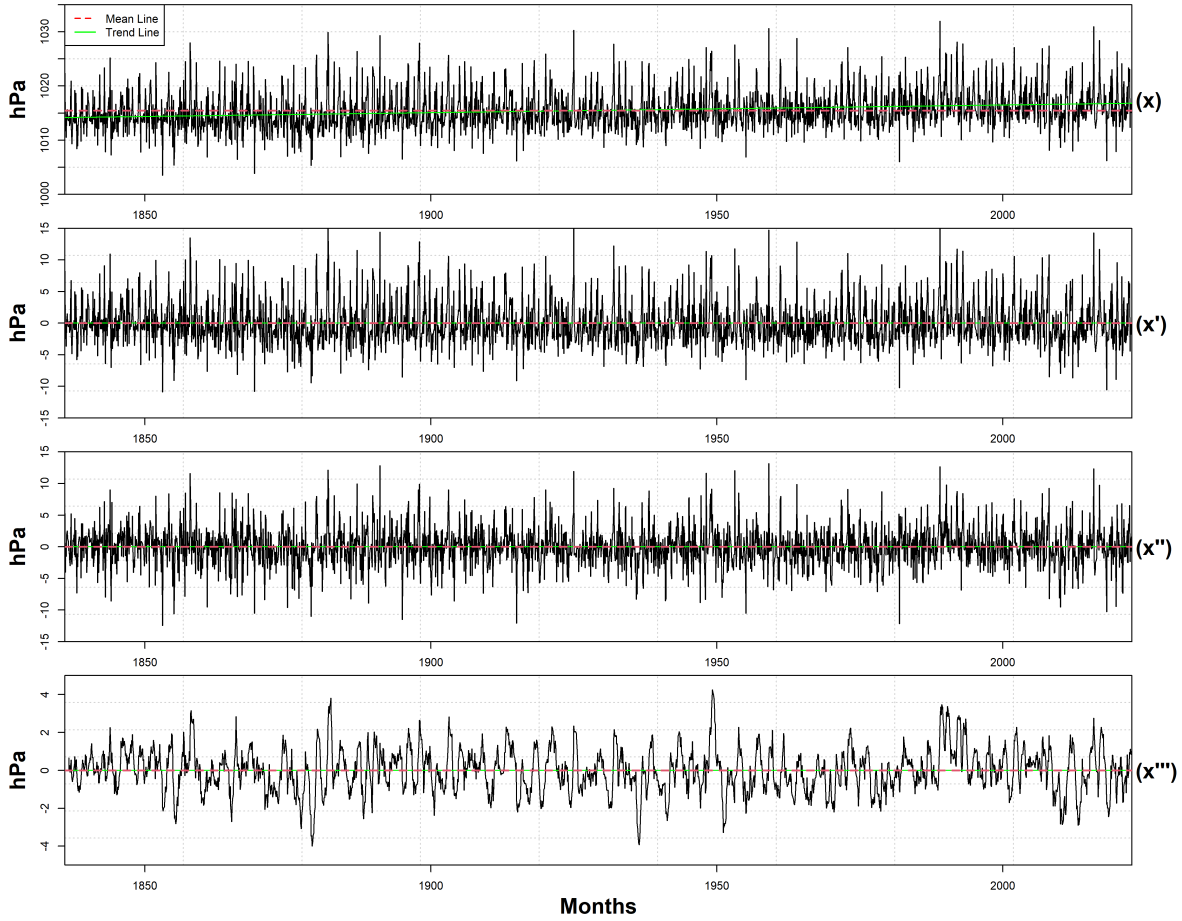

Figure S2. Example of the results at each step applied to obtain anomalies (SLP over Genova) time series of raw data (x), detrended data (x'), seasonality removed data (x"), and moving average applied data (x"').

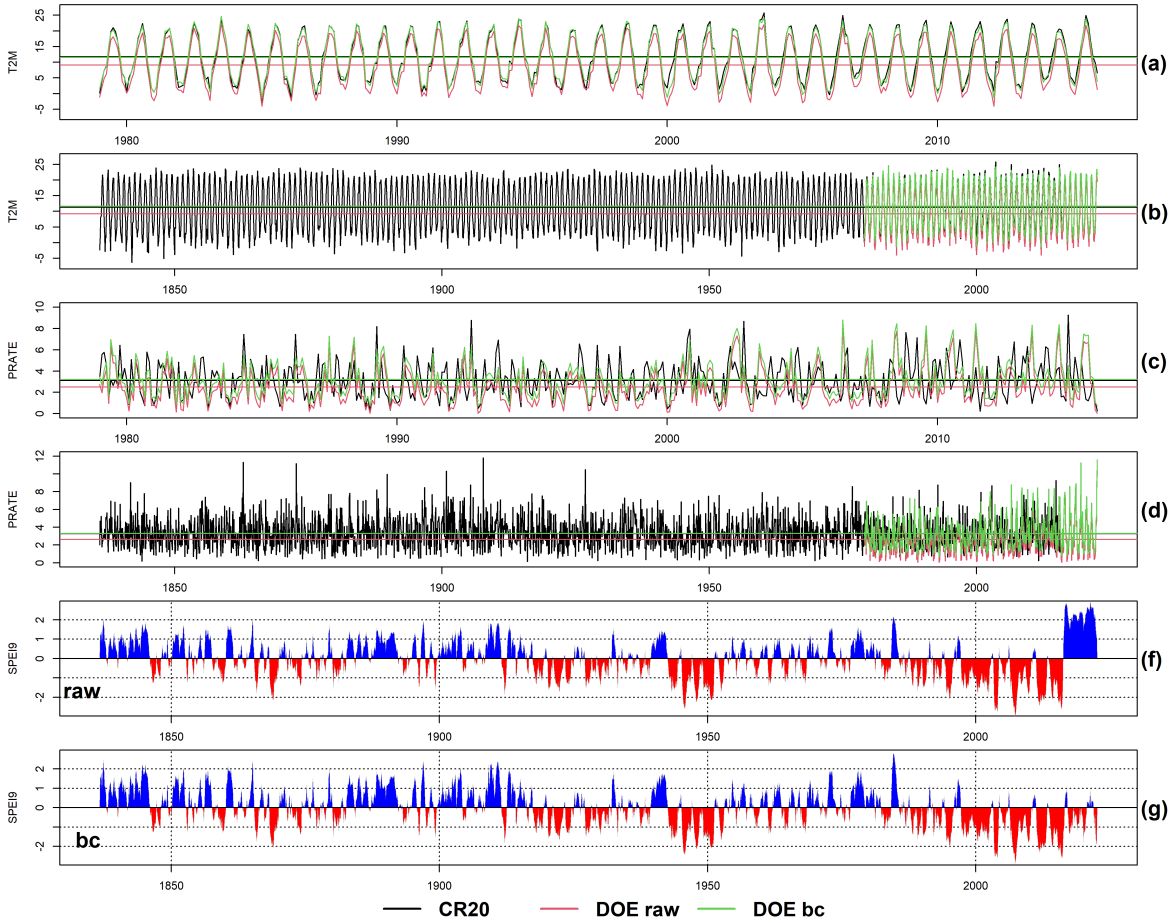

Figure S3. Comparisons of the time series obtained by combining 20CR and raw/bias-corrected NCEP/DOE T2M and PRATE time series for the common period (a,c) and complete study period (b,d), SPEI9 time series obtained from raw input datasets (e) and bias-corrected datasets (f) obtained over Genova. CR20, raw, and bias-corrected NCEP/DOE time series are shown in black, red, and green colors, respectively.

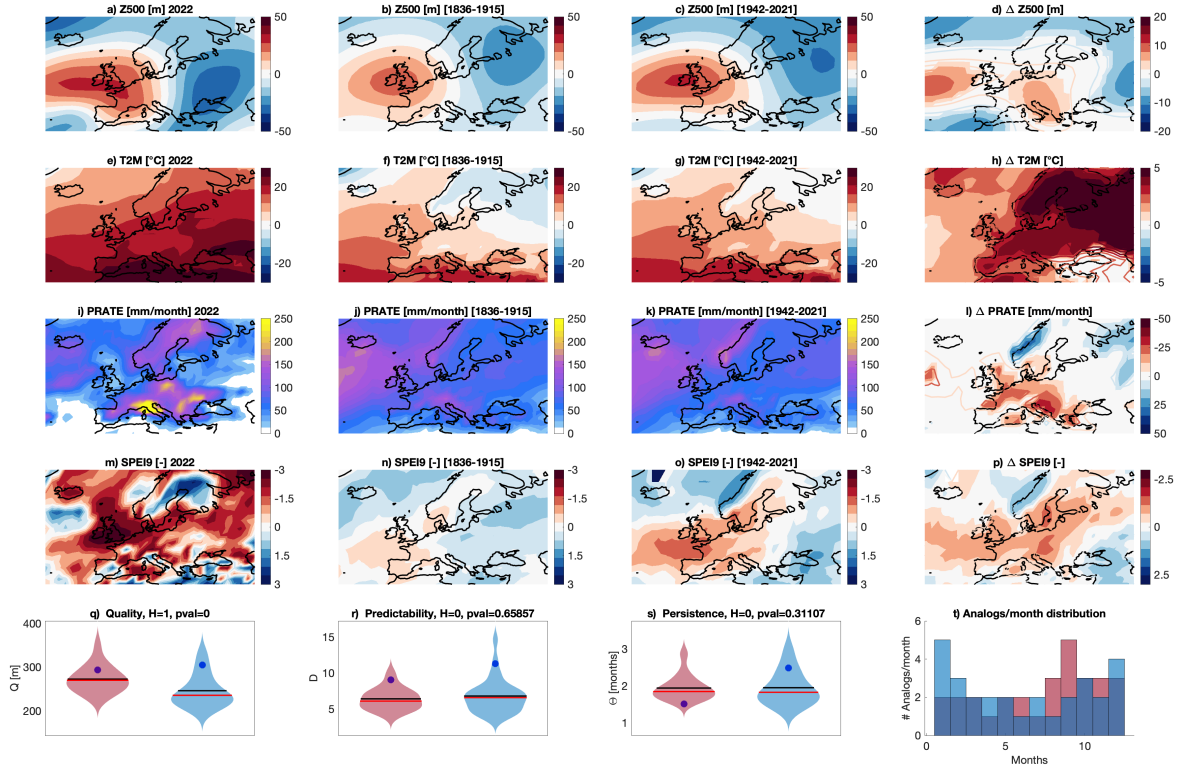

Figure S4. Attribution results for the 2022 Drought via analogs. As in Figure 2 in the main text, but for analogs of the non-bias corrected 500 geopotential height and the DOE dataset.

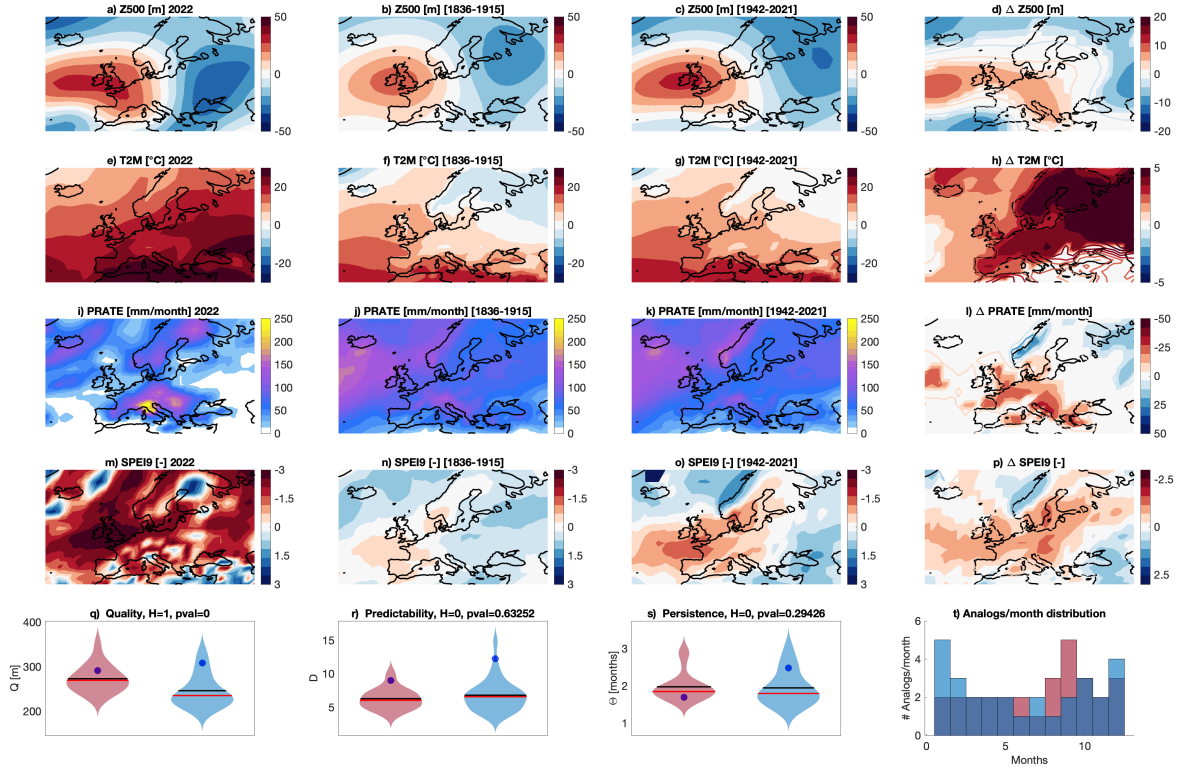

Figure S5. Attribution results for the 2022 Drought via analogs. As in Figure 2 in the main text, but for analogs of the non-bias corrected 500 geopotential height and the NCAR dataset.

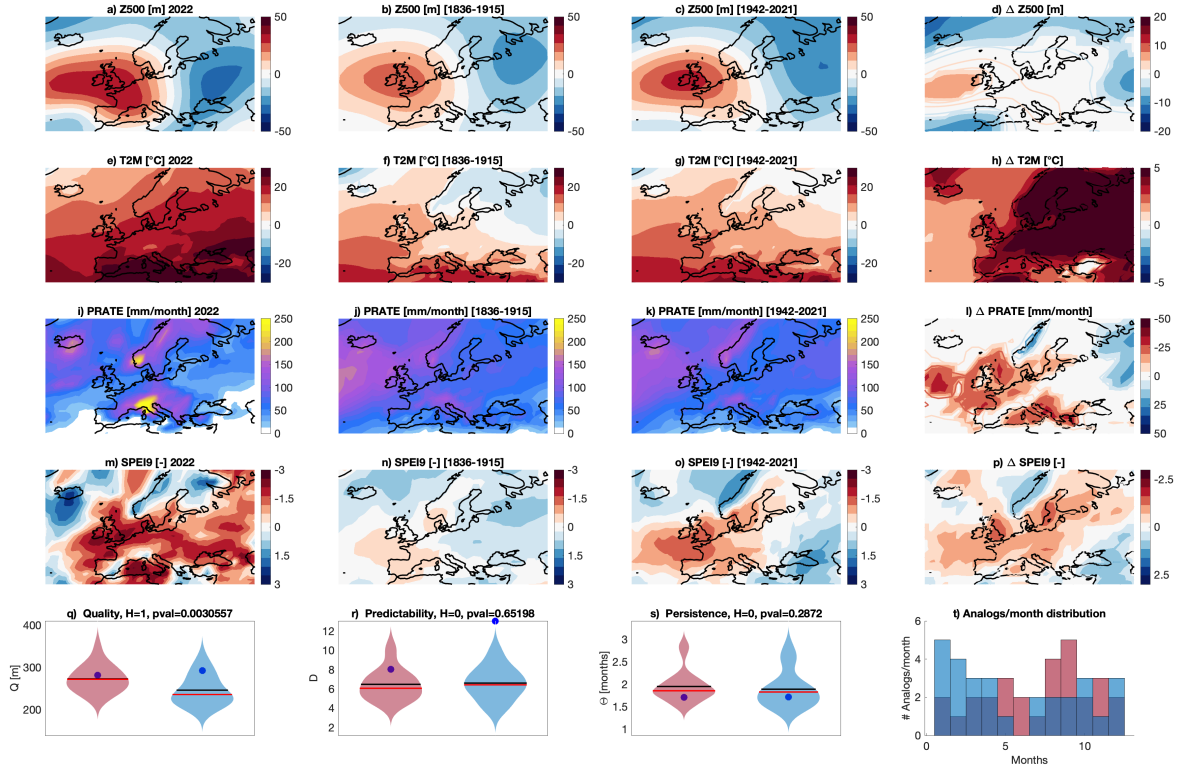

Figure S6. Attribution results for the 2022 Drought via analogs. As in Figure 2 in the main text, but for analogs of the bias corrected 500 geopotential height and the NCAR dataset.

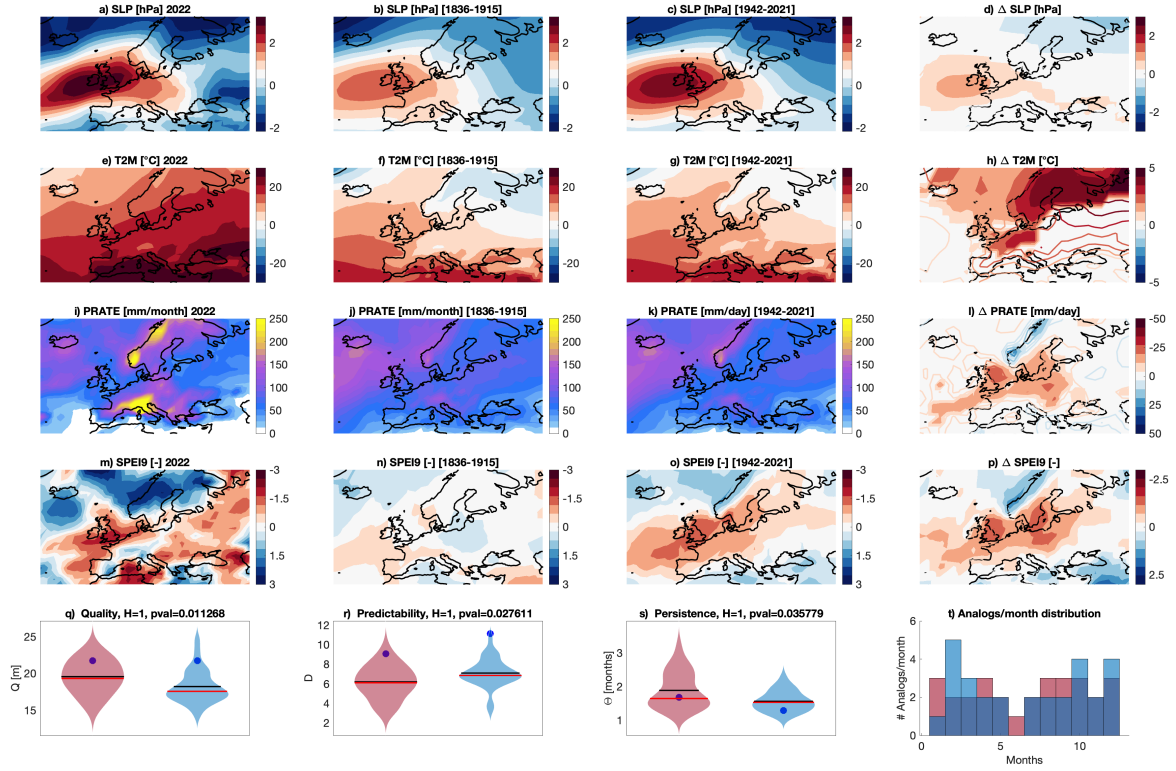

Figure S7. Attribution results for the 2022 Drought via analogs. As in Figure 2 in the main text, but for analogs of the bias corrected sea-level pressure and the DOE dataset.

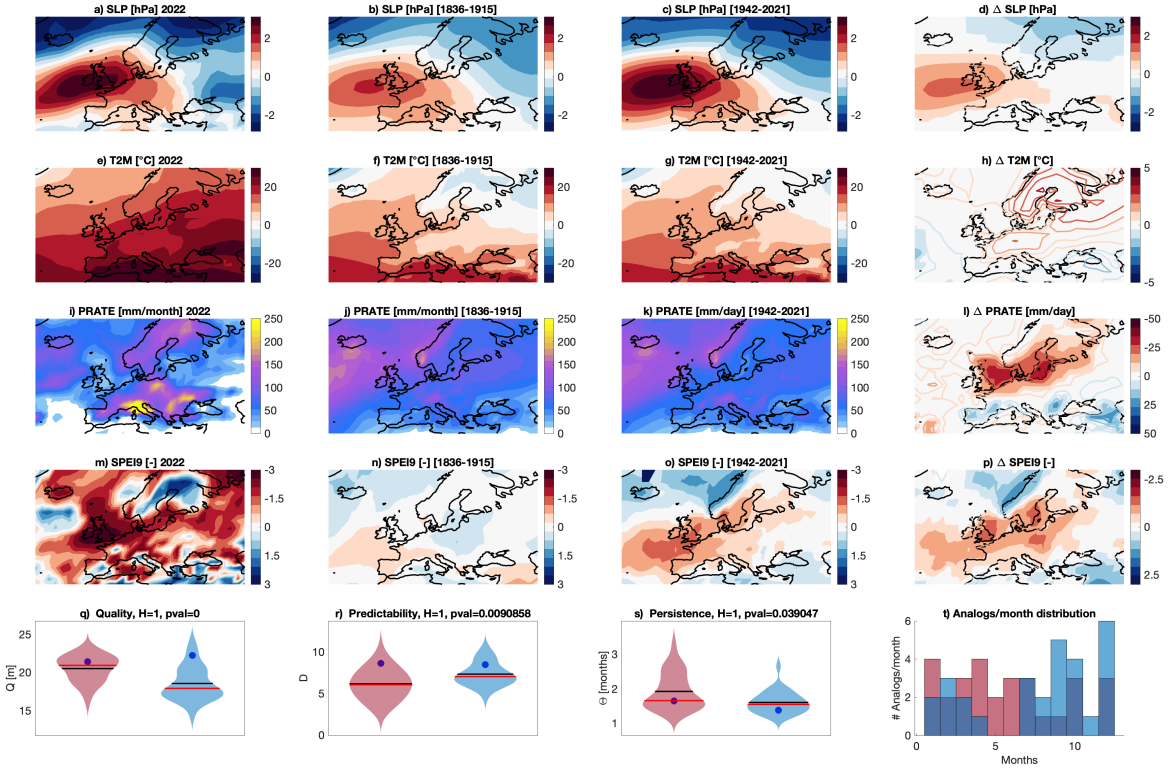

Figure S8. Attribution results for the 2022 Drought via analogs. As in Figure 2 in the main text, but for analogs of the non bias-corrected sea-level pressure and the DOE dataset.

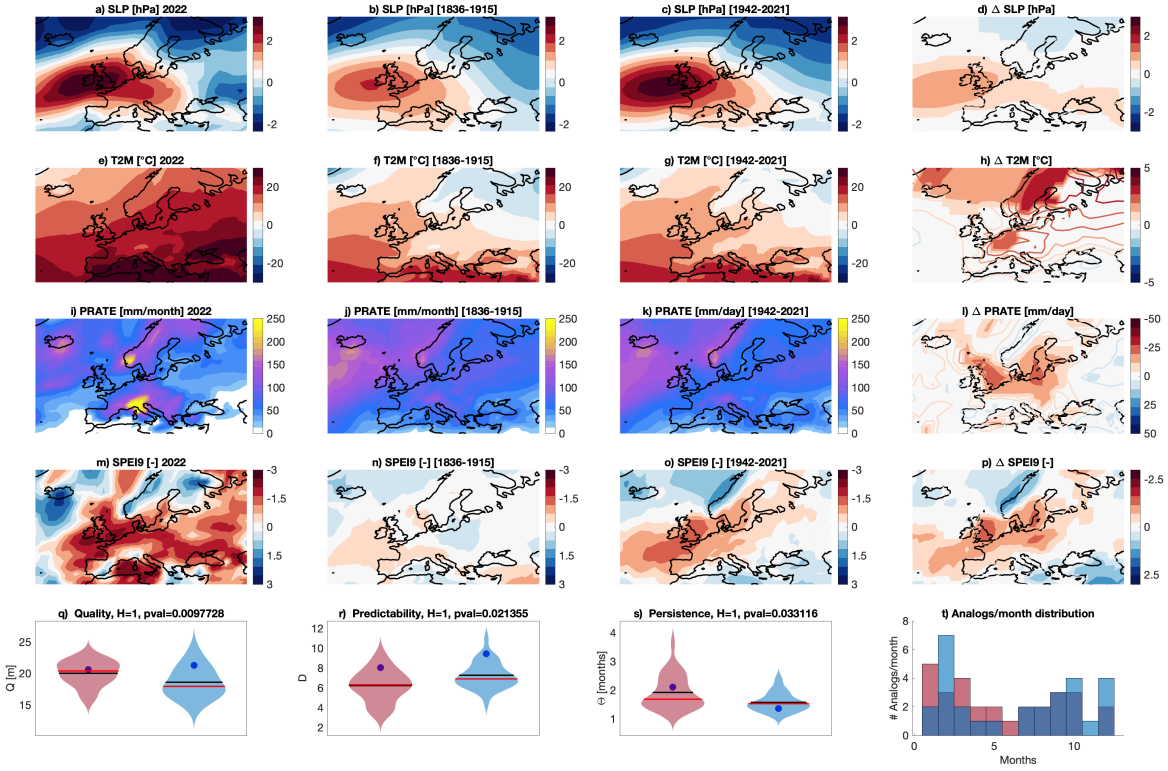

Figure S9. Attribution results for the 2022 Drought via analogs. As in Figure 2 in the main text, but for analogs of the bias corrected sea-level pressure and the NCAR dataset.

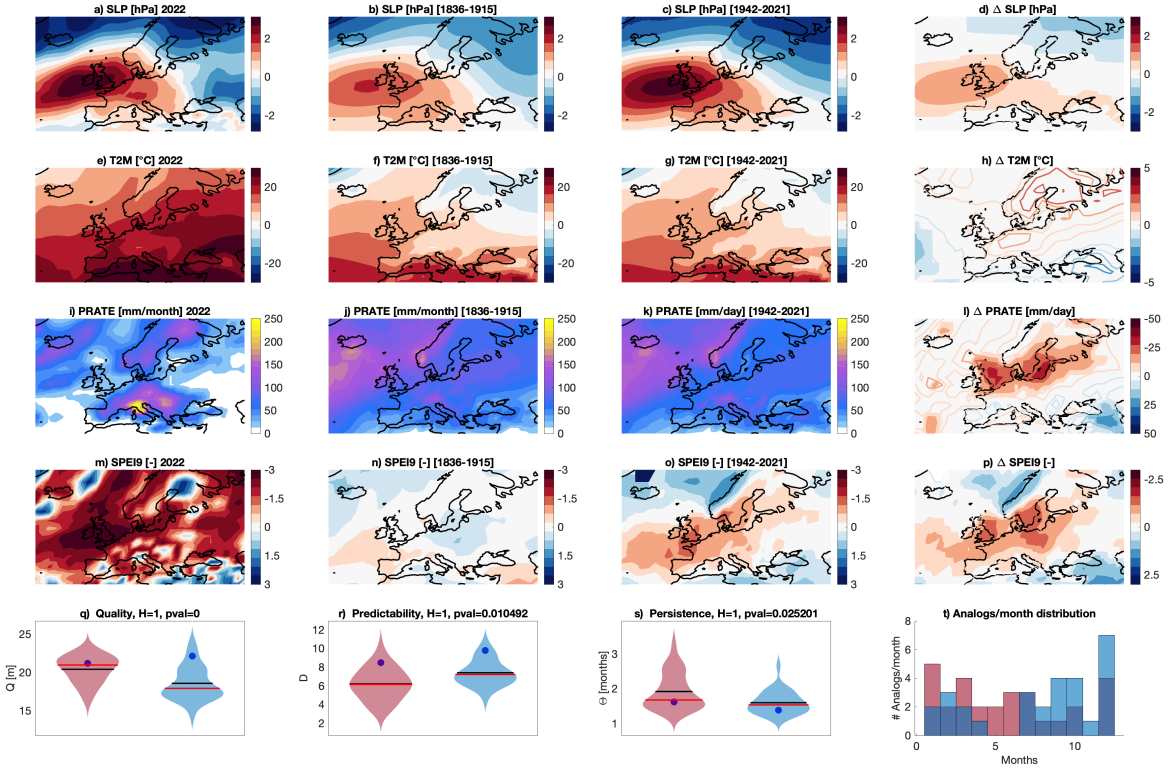

Figure S10. Attribution results for the 2022 Drought via analogs. As in Figure 2 in the main text, but for analogs of the non bias-corrected sea-level pressure and the NCAR dataset.

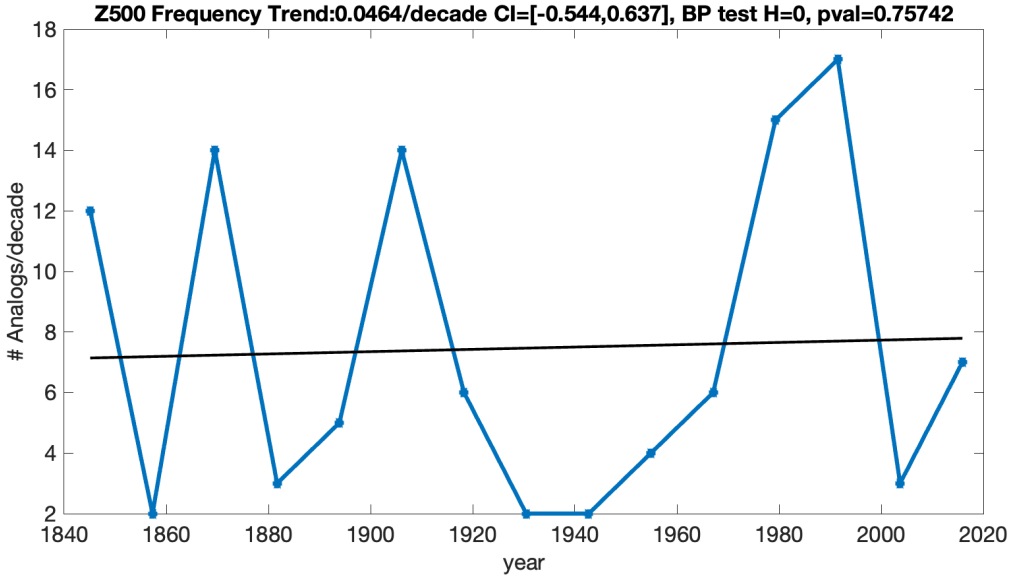

Figure S11. Evolution of the Frequency of analogs in time. As in Figure 3 in the main text, but for analogs of the non-bias corrected 500 geopotential height and the DOE dataset.

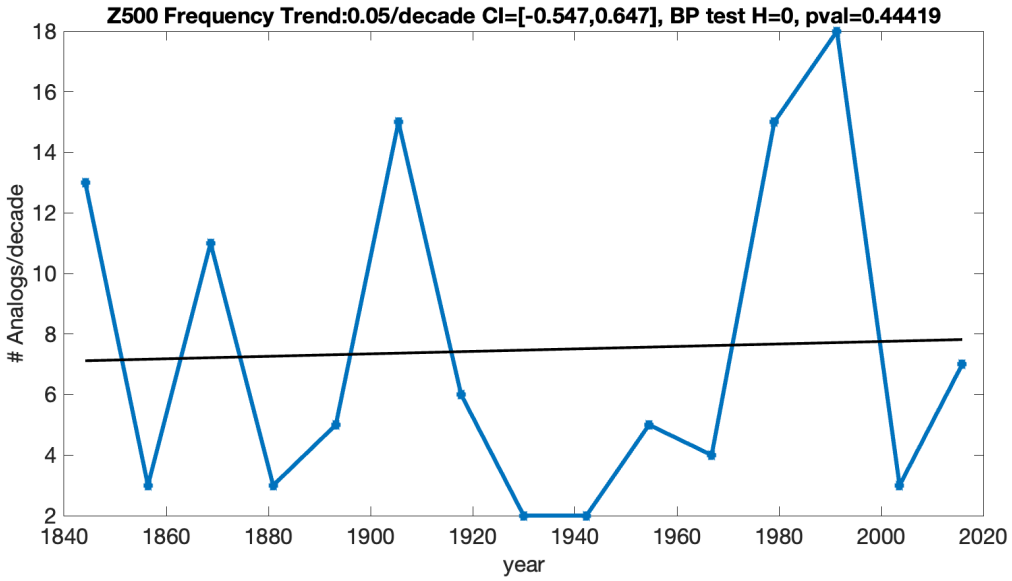

Figure S12. Evolution of the Frequency of analogs in time. As in Figure 3 in the main text, but for analogs of the non-bias corrected 500 geopotential height and the NCAR dataset.

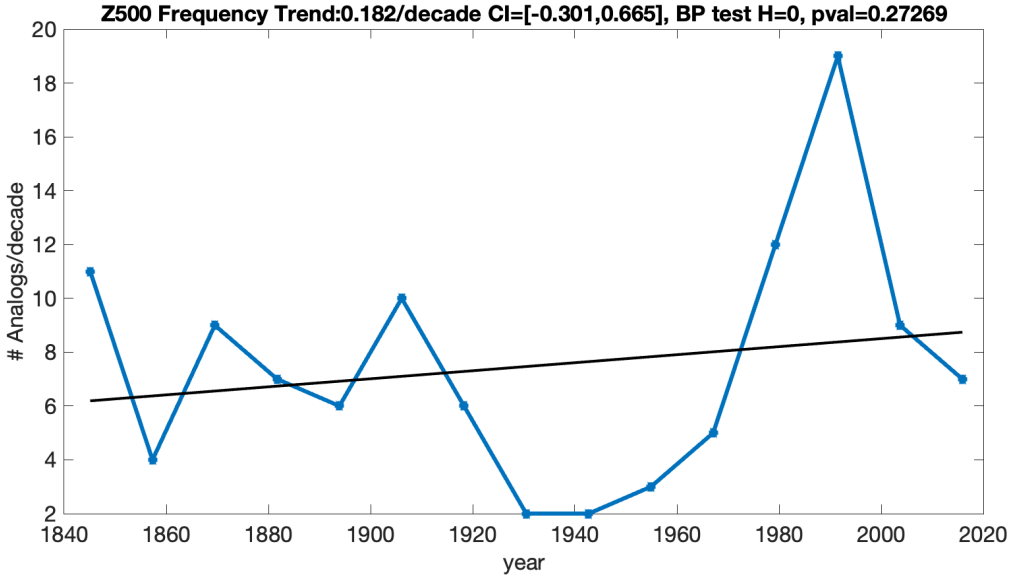

Figure S13. Evolution of the Frequency of analogs in time. As in Figure 3 in the main text, but for analogs of the bias corrected 500 geopotential height and the NCAR dataset.

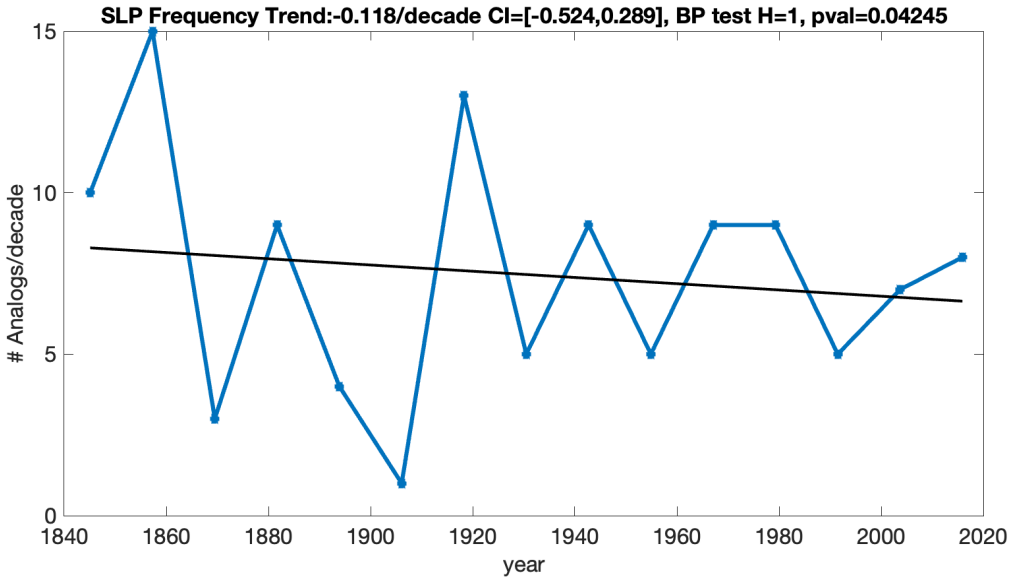

Figure S14. Evolution of the Frequency of analogs in time. As in Figure 3 in the main text, but for analogs of the bias corrected sea-level pressure and the DOE dataset.

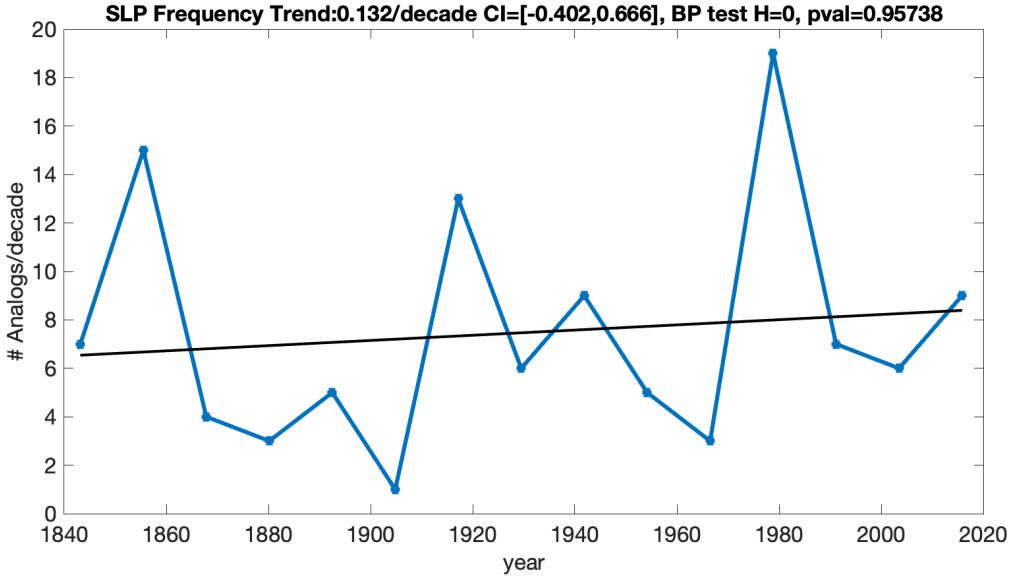

Figure S15. Evolution of the Frequency of analogs in time. As in Figure 3 in the main text, but for analogs of the non bias-corrected sea-level pressure and the DOE dataset.

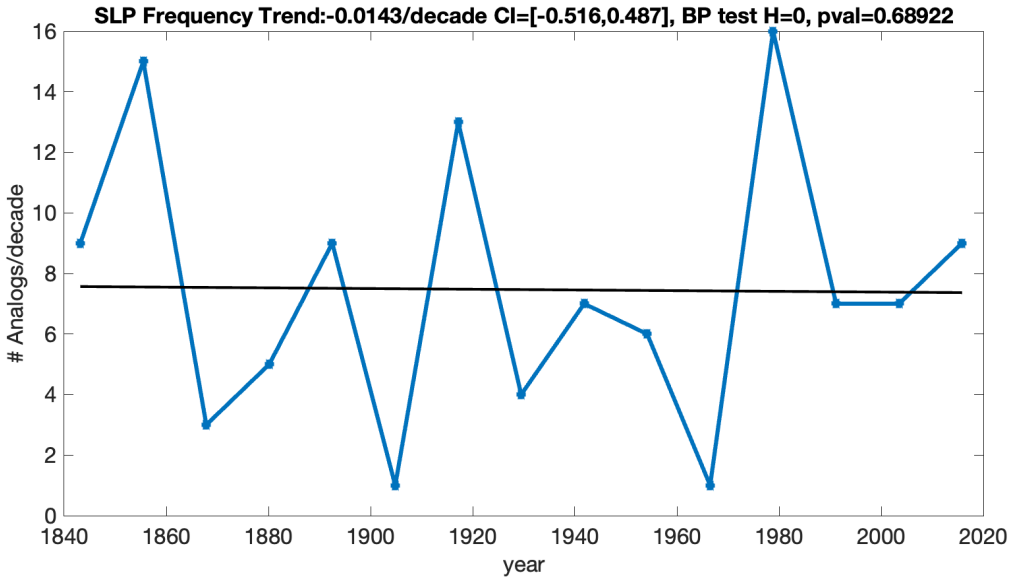

Figure S16. Evolution of the Frequency of analogs in time. As in Figure 3 in the main text, but for analogs of the bias corrected sea-level pressure and the NCAR dataset.

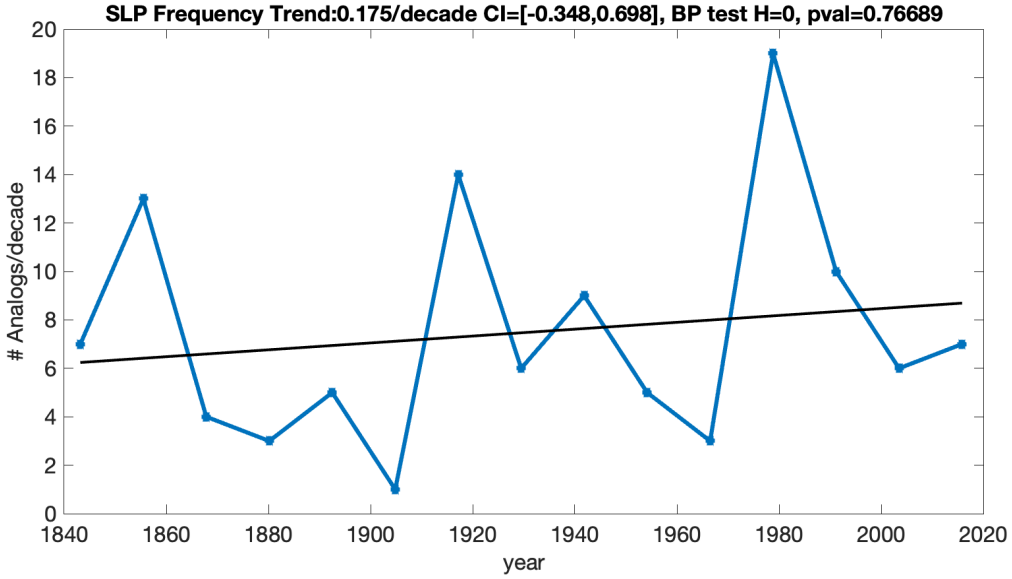

Figure S17. Evolution of the Frequency of analogs in time. As in Figure 3 in the main text, but for analogs of the non bias-corrected sea-level pressure and the NCAR dataset.

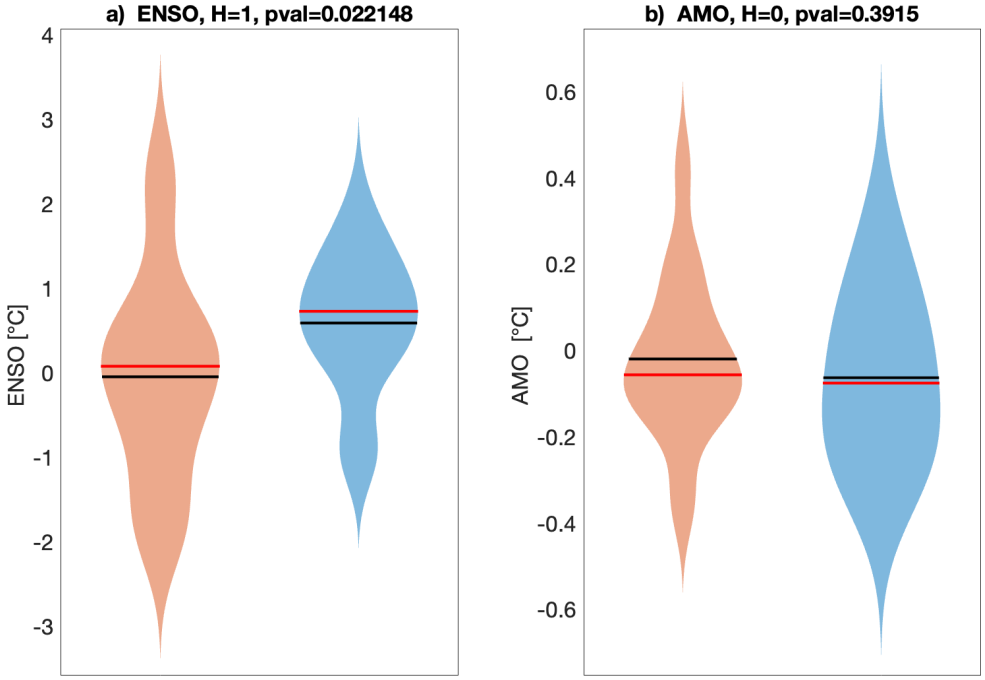

Figure S18. Analysis of the Interannual and Interdecadal variability. As in Figure 4 in the main text, but for analogs of the non-bias corrected 500 geopotential height and the DOE dataset.

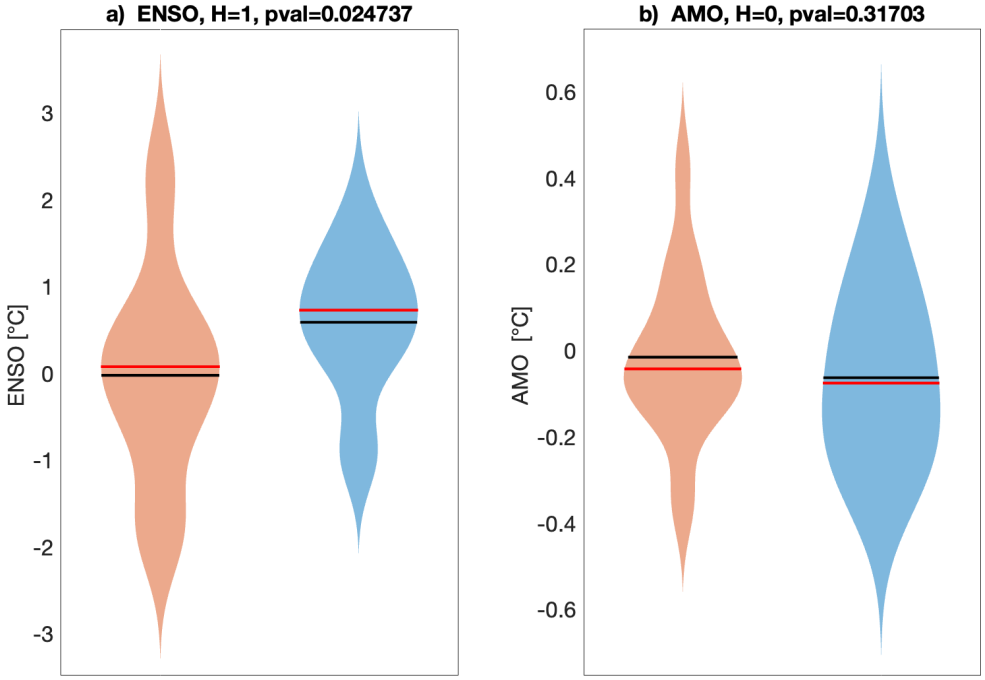

Figure S19. Analysis of the Interannual and Interdecadal variability. As in Figure 4 in the main text, but for analogs of the non-bias corrected 500 geopotential height and the NCAR dataset.

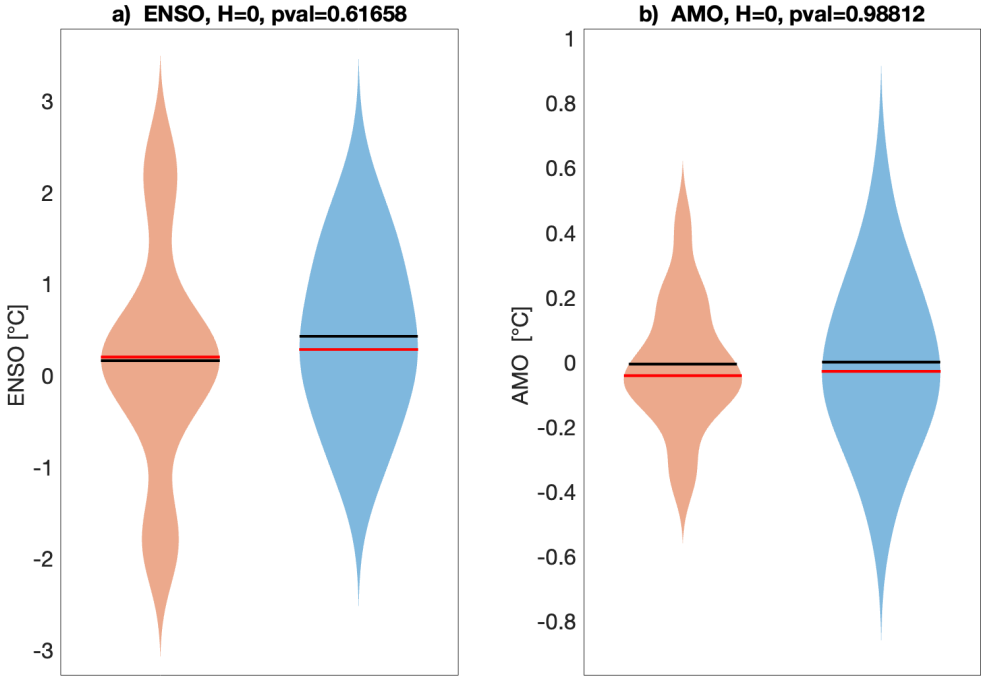

Figure S20. Analysis of the Interannual and Interdecadal variability. As in Figure 4 in the main text, but for analogs of the bias corrected 500 geopotential height and the NCAR dataset.

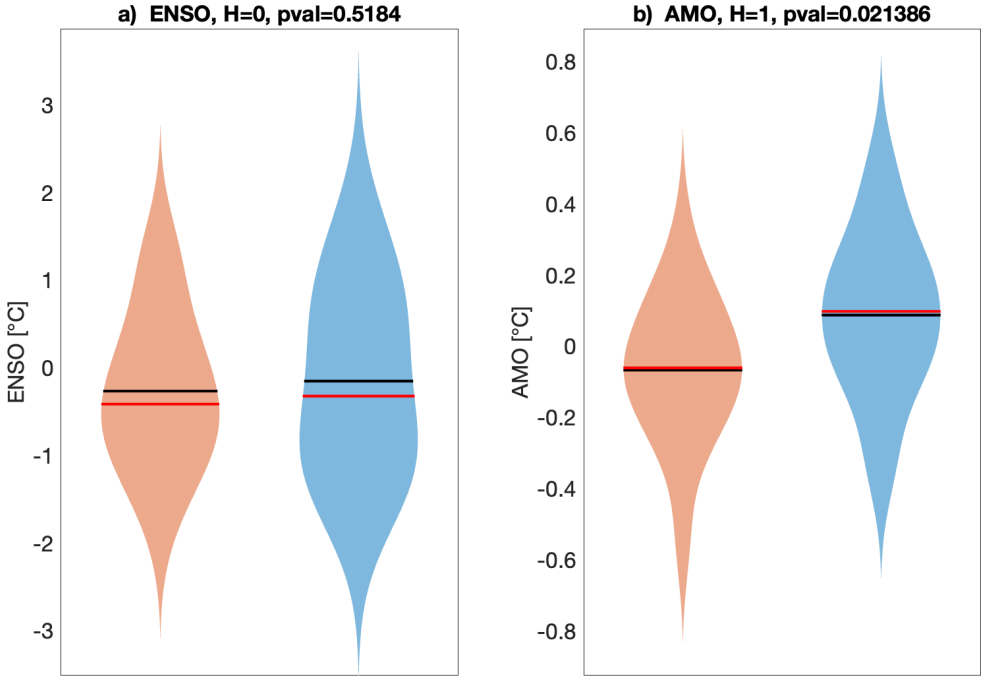

Figure S21. Analysis of the Interannual and Interdecadal variability. As in Figure 4 in the main text, but for analogs of the bias corrected sea-level pressure and the DOE dataset.

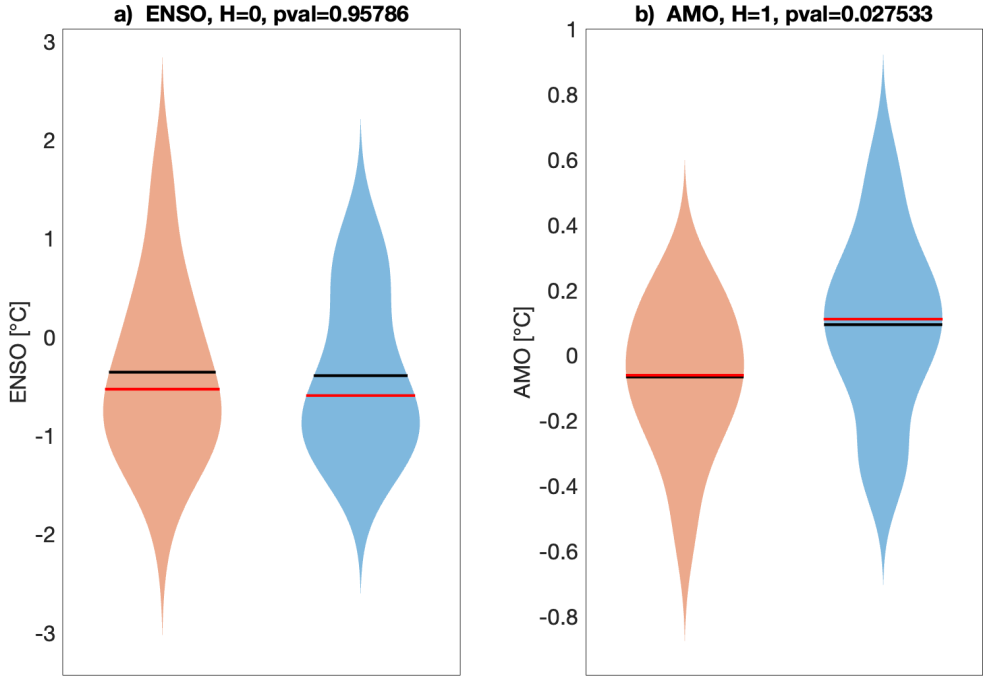

Figure S22. Analysis of the Interannual and Interdecadal variability. As in Figure 4 in the main text, but for analogs of the non bias-corrected sea-level pressure and the DOE dataset.

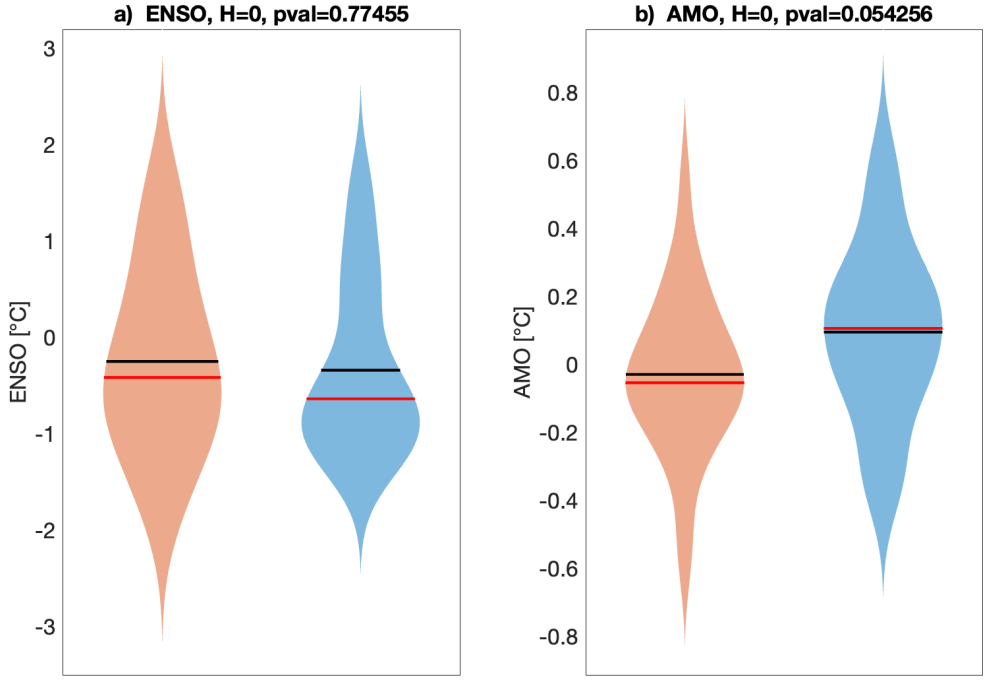

Figure S23. Analysis of the Interannual and Interdecadal variability. As in Figure 4 in the main text, but for analogs of the bias corrected sea-level pressure and the NCAR dataset.

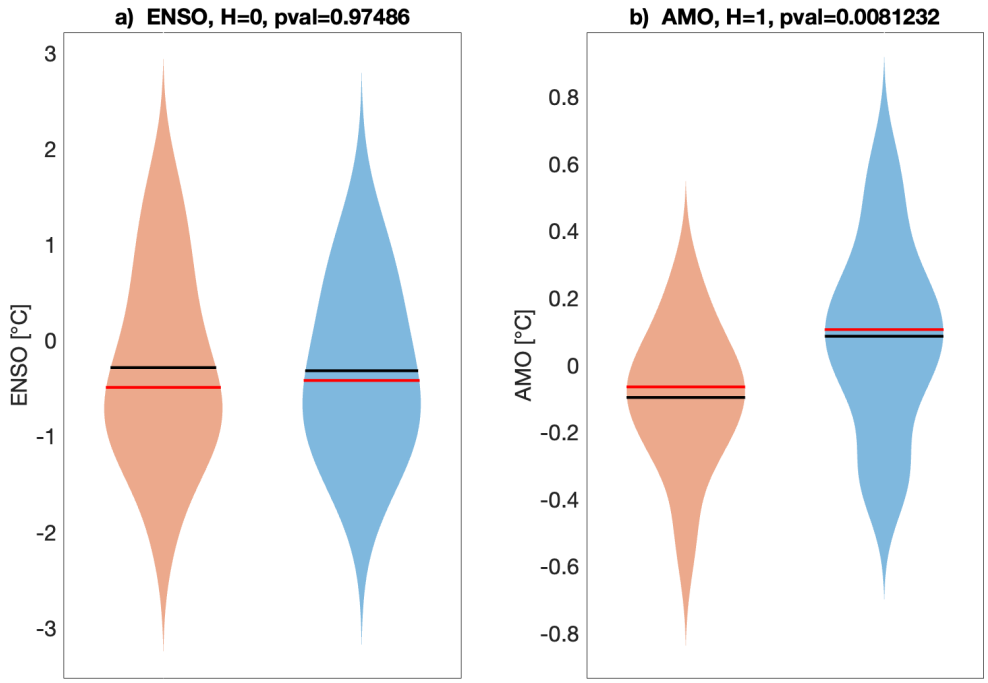

Figure S24. Analysis of the Interannual and Interdecadal variability. As in Figure 4 in the main text, but for analogs of the non bias-corrected sea-level pressure and the NCAR dataset.

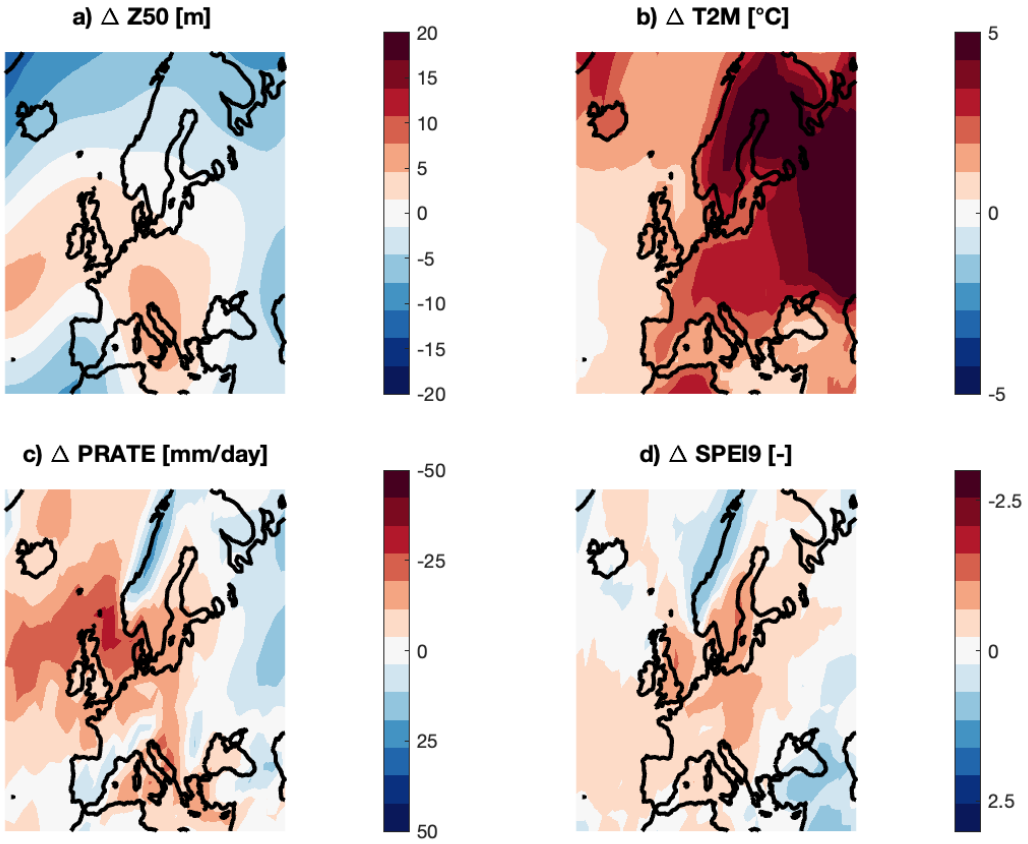

Figure S25. Average of the Z500 attribution results obtained for the individual 20CRv3 ensemble members. Average for ΔZ500 (a), ΔT2M (b), Δ PRATE (c) and ΔSPEI9 (d) obtained by analysing individually single members of the 20CRv3 ensemble completed with the bias-corrected DOE dataset.

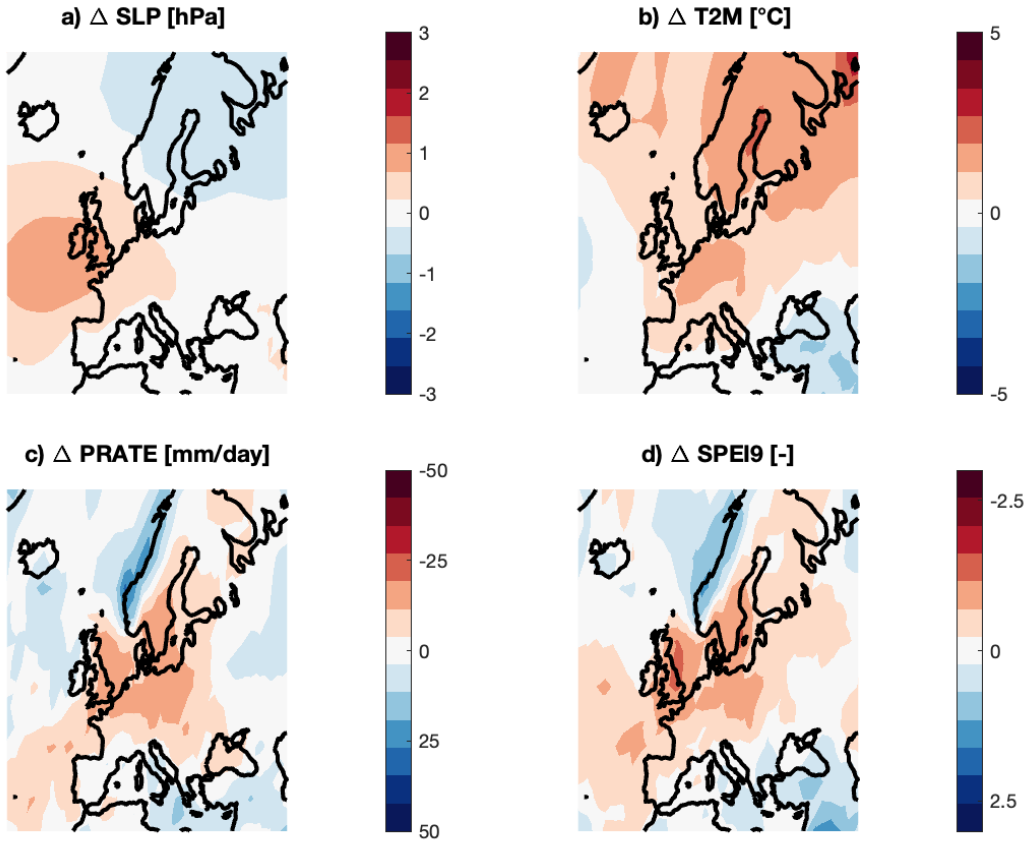

Figure S26. Average of the SLP attribution results obtained for the individual 20CRv3 ensemble members. Average for ΔSLP (a), ΔT2M (b), Δ PRATE (c) and ΔSPEI9 (d) obtained by analysing individually single members of the 20CRv3 ensemble completed with the bias-corrected DOE dataset.

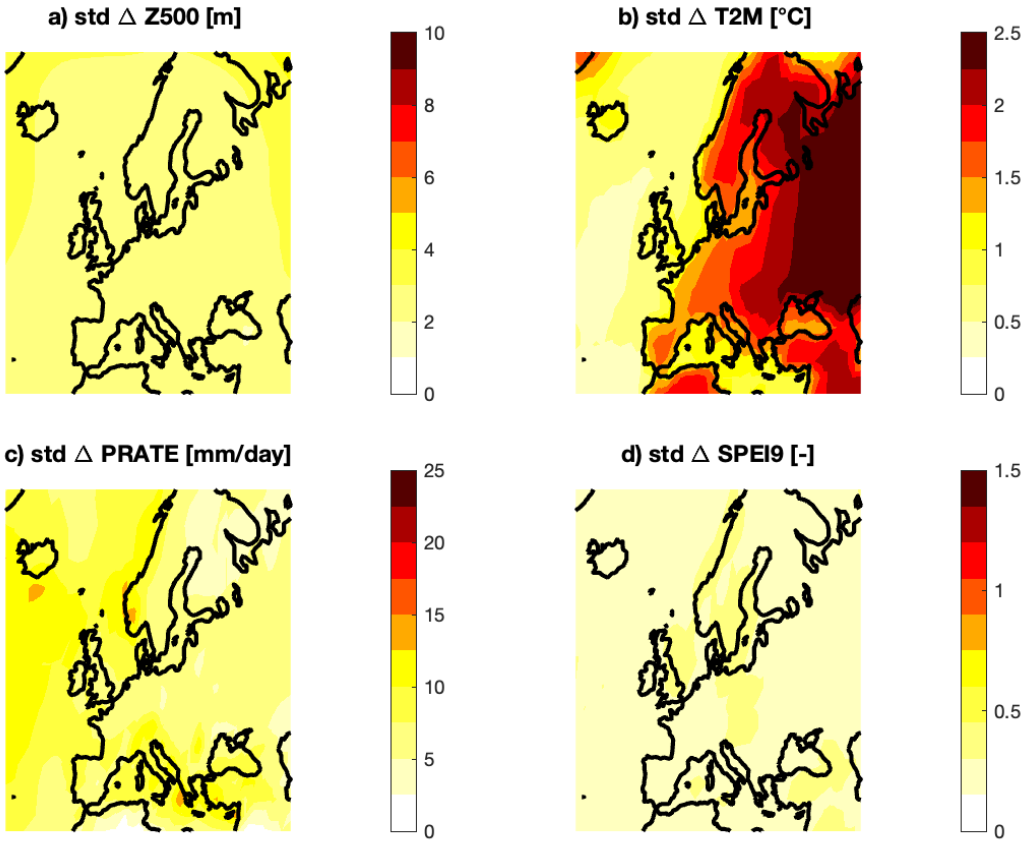

Figure S27. Standard Deviation of the Z500 attribution results obtained for the individual 20CRv3 ensemble members. Standard deviation for ΔZ500 (a), ΔT2M (b), Δ PRATE (c) and ΔSPEI9 (d) obtained by analysing individually single members of the 20CRv3 ensemble completed with the bias-corrected DOE dataset.

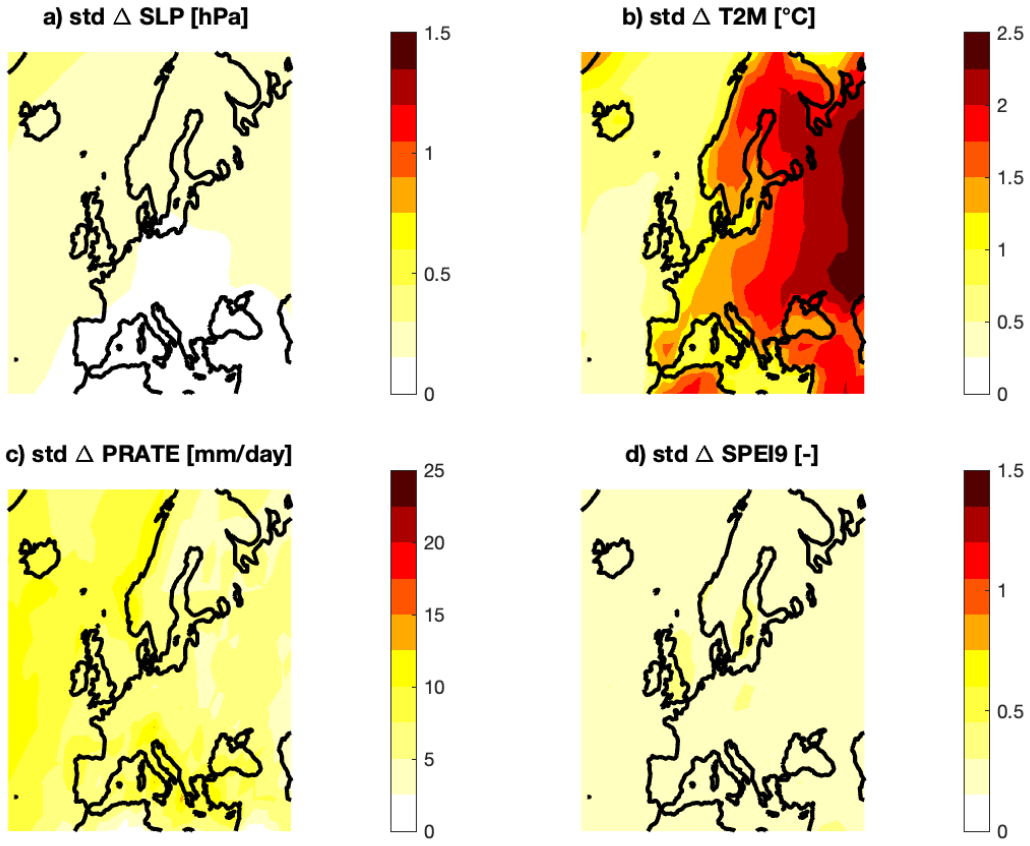

Figure S28. Standard Deviation of the SLP attribution results obtained for the individual 20CRv3 ensemble members. Standard deviation for ΔSLP (a), ΔT2M (b), Δ PRATE (c) and ΔSPEI9 (d) obtained by analysing individually single members of the 20CRv3 ensemble completed with the bias-corrected DOE dataset.